Transport and mixing in the extratropical tropopause region in a high vertical resolution GCM. Part II: Relative importance of large-scale and small-scale dynamics

Kazuyuki Miyazaki *

Research Institute for Global Change, Japan Agency for Marine-Earth Science and Technology, Yokohama, Japan

Kaoru Sato

Department of Earth and Planetary Science, Graduate School of Science, University of Tokyo, Tokyo, Japan

Shingo Watanabe

Research Institute for Global Change, Japan Agency for Marine-Earth Science and Technology, Yokohama, Japan

Yoshihiro Tomikawa

National Institute of Polar Research, Tokyo, Japan

Yoshio Kawatani

Research Institute for Global Change, Japan Agency for Marine-Earth Science and Technology, Yokohama, Japan

Masaaki Takahashi

Center for Climate System Research, University of Tokyo, Kashiwa, Japan

* *Corresponding author address:* Kazuyuki Miyazaki, Research Institute for Global Change, Japan Agency for Marine-Earth Science and Technology, 3173-25 Showa-machi, Kanazawa-ku, Yokohama, Japan 236-0001.

E-mail: kmiyazaki@jamstec.go.jp

ABSTRACT

The relative roles of atmospheric motions on various scales, from meso-wave scale to planetary scale, in transport and mixing in the extratropical tropopause region are investigated using a high-vertical-resolution general circulation model (GCM). The GCM with a vertical resolution of about 300 m explicitly represents the propagation and breaking of gravity waves and the induced transport and mixing. A downward control calculation shows that the Eliassen-Palm (E-P) flux of the gravity waves diverges and induces a mean equatorward flow in the extratropical tropopause region, which differs from the mean poleward flow induced by the convergence of large-scale E-P fluxes. The diffusion coefficients estimated from the eddy potential vorticity flux in tropopause-based coordinates reveal that isentropic motions diffuse air between 20 K below and 10 K above the tropopause from late autumn to early spring, while vertical mixing is strongly suppressed at around 10-15 K above the tropopause throughout the year. The isentropic mixing is mainly caused by planetary- and synoptic-scale motions, while small-scale motions with a horizontal scale of less than a few thousand kilometer largely affect the three-dimensional mixing just above the tropopause. Analysis of the gravity wave energy and atmospheric instability implies that the small-scale dynamics associated with the dissipation and saturation of gravity waves are a significant cause of the three-dimensional mixing just above the tropopause. A rapid increase in the static stability in the tropopause inversion layer is considered to play an important role in controlling the gravity wave activity around the tropopause.

1. INTRODUCTION

In a companion paper (Miyazaki et al., 2009), we examined the roles of dynamic and thermodynamic processes in maintaining the extratropical transition layer (ExTL) and the tropopause inversion layer (TIL). A large vertical temperature gradient in the lowermost stratosphere forms the TIL (Birner et al., 2002), while chemical constituent concentrations in the ExTL are intermediate to those typical in the troposphere and stratosphere (Fischer et al., 2000; Hoor et al., 2004). These two layers are known to be almost collocated just above the extratropical tropopause (e.g., Hegglin et al., 2009). The analysis used a vertically highly resolved general circulation model (GCM) that had a horizontal resolution of T213 and a vertical resolution of about 300 m above the extratropical upper troposphere. The high-resolution GCM was capable of realistically simulating atmospheric fine-scale structures in the extratropical upper troposphere and lower stratosphere (UTLS), including the ExTL and TIL. From a potential vorticity (PV) and thermodynamic balance analysis, we found that the ExTL and TIL can have similar locations, as a result of common dynamic processes and interactions between their constituent distributions and thermal structures in the extratropical tropopause region; i.e. downward advection of constituent concentration gradients and heat at the lower part of these layers, and the mixing of constituents (including water vapor) and radiative stratification effects related to large constituent concentration gradients at the upper part of these layers. Although Miyazaki et al. (2009) provided insight into the atmospheric processes in the extratropical tropopause region, their relative importance at different spatiotemporal scales has not yet been discussed.

Planetary-scale and synoptic-scale waves are known to be important in determining atmo-

spheric structures and constituent distributions in the extratropical UTLS. Planetary-scale waves cause significant mixing within the stratospheric surf zone (McIntyre and Palmer, 1984) and induce a poleward and downward mean-meridional circulation (i.e., Brewer-Dobson circulation) in the extratropical stratosphere (e.g., Rosenlof and Holton, 1993). The mean downward motion induced by planetary waves provides an important transport pathway to the extratropical tropopause region from higher levels. Synoptic-scale waves (e.g., baroclinic waves) cause significant transport and mixing in the upper troposphere and around the tropopause in the extratropics (e.g., Stone et al., 1999). The exchange of air caused by these large-scale motions across the tropopause plays an essential role in the abundance of chemical constituents in both the troposphere and stratosphere (Holton et al., 1995): for example, the stratosphere-troposphere exchange (STE) on the isentropic surface is mainly due to mixing by Rossby wave breaking and stirring effects by differential advection near the jet stream (e.g., Chen et al., 1994; Postel and Hitchman, 1999, 2001). Moreover, medium-scale waves, with a typical zonal wavelength of 2000-3000 km, also affect the circulation near the mid-latitude tropopause. Active medium-scale waves have been observed in spring at slightly higher latitudes than the subtropical jet stream (Sato et. al., 1993; Yamamori et. al., 1997).

In addition to large-scale and medium-scale motions, small-scale motions by turbulence and gravity wave breaking play important roles in transporting air around the extratropical tropopause (e.g., Clark and Peltier, 1977; Shapiro, 1980; Lane et al., 2003; Pavelin et al. 2002). Gravity wave saturation processes play roles in determining the spectrum of atmospheric motions and lead to small-scale motions. Gravity wave breaking results in three-dimensional turbulence and mixing (e.g., Fritts and Alexander, 2003). Gravity wave

momentum fluxes act to accelerate (or decelerate) large-scale flows at levels where gravity waves are transient or dissipating through wave-mean flow interactions. Turbulence dominates very small-scale motions around the tropopause, particularly at scales of less than several km (Duck and Whiteway, 2005). Observational studies have found strong gravity wave activity around and just above the tropopause (e.g., Allen and Vincent, 1995; Lamarque et al., 1996; Lane and Sharman, 2008; Schmidt et al., 2008). Lamarque et al. (1996) demonstrated that the topographically excited gravity waves that break at the tropopause level are responsible for irreversible mixing across the tropopause over a mountainous region. Lane and Sharman (2008) showed that gravity wave breaking dominate a turbulent generation above a deep convection, in which the critical level of this gravity wave breaking is controlled by the above-cloud wind shear. At the same time, an important source of inertia-gravity waves is located near the tropopause level at atmospheric jets (e.g., Plougonven and Snyder, 2005; 2007). Rapid changes in the static stability around the TIL can obviously affect the small-scale dynamics related to the propagation and breaking of gravity waves (e.g., VanZandt and Fritts, 1989). The small-scale dynamics may provide significant contributions to transport and mixing processes in the extratropical tropopause region.

High-vertical-resolution GCMs with no gravity wave drag parameterizations can explicitly represent the propagation and breaking of gravity waves and the induced wave-mean flow interactions. In this paper, we analyze the output of a high-vertical-resolution GCM to demonstrate the relative importance of atmospheric motions with various scales, from the gravity wave-scale to planetary-scale, on transport and mixing in the extratropical tropopause region. The structure of this paper is as follows. In Section 2, we describe a high-vertical-resolution GCM and the analysis methods for the downward control calcula-

tion and diffusion coefficients. Section 3 presents the relative roles of waves of various scales in driving the mean-meridional circulation. In Section 4, we present the mixing characteristics in the extratropical tropopause region and the relative contributions of atmospheric motions with different spatial scales to this mixing. In Section 5, we discuss the gravity wave activity in the extratropical tropopause region. Conclusions are given in Section 6.

2. Methodology

a. Description of a T213L256 GCM

We adopted a high-vertical-resolution GCM developed by Watanabe et al. (2008) to investigate the transport and mixing processes in the extratropical UTLS. This GCM has been used to survey various small-scale phenomena, including gravity waves and their role in large-scale circulation fields in the atmosphere (Watanabe et al., 2008, 2009; Tomikawa et al., 2008; Miyazaki et al., 2009; Sato et al., 2009). The GCM has a T213 truncation in the horizontal (i.e., latitude-longitude grid intervals of 0.5625°) direction and 256 levels in the vertical direction, from the surface to about 85 km, with a vertical resolution of about 300 m above the extratropical upper troposphere through the middle atmosphere. The aspect ratio of the horizontal to vertical resolution (~ 300) may be very appropriate for the UTLS as discussed in Birner (2006). Gravity waves are explicitly simulated in this high-vertical-resolution GCM, with no gravity wave drag parameterizations, for both orographic and non-orographic components. The high-vertical-resolution allows us to resolve a large portion of the observed gravity waves; their typical vertical wavelengths are 1-4 km in the

lower stratosphere (Sato, 1994; Sato et al., 1997). Although the high-vertical-resolution GCM makes it possible to study various small-scale phenomena including gravity waves, it still misses a great deal of the GW spectrum (scales smaller than a few hundred kilometers).

Miyazaki et al. (2009) demonstrated that the high-vertical-resolution GCM simulated reasonably the thermal and dynamical fine-scale structure around the extratropical tropopause region. The thickness and maximum stability of the TIL was much better represented in the high-vertical-resolution GCM than in a standard resolution GCM (with a horizontal resolution of T42 and 32 vertical levels from the surface to the upper stratosphere). Further details of the GCM are given in Watanabe et al. (2008). The results of the analysis using hourly GCM ouput are presented as fields averaged overt there years.

b. Analysis methods

1) Downward control calculation

The Eliassen-Palm (E-P) flux divergence drives the mean-meridional circulation through wave-mean flow interactions. The relationship can be diagnosed from the downward control principle (Haynes et al. 1991) for steady-state conditions in the transformed Eulerian mean (TEM) framework (Andrews and McIntyre, 1976):

$$\psi = \int_z^\infty \left(\frac{\rho_0 a^2 \mathcal{F} \cos^2 \phi}{\overline{m}_\phi} \right)_{\phi=\phi(z')} dz', \tag{1}$$

$$\overline{w^*} = \frac{1}{\rho_0 \cos\phi} \frac{\partial}{\partial \phi} \int_z^\infty \left(\frac{\rho_0 a \mathcal{F} \cos^2 \phi}{\overline{m}_\phi} \right)_{\phi=\phi(z')} dz', \tag{2}$$

where ψ is the streamfunction, $\overline{w^*}$ is the mean vertical velocity, $\mathcal{F}$ is the divergence of the E-P flux estimated in the TEM framework, a is the Earth's radius, $\rho_0 = \exp(-z/H)$

is the atmospheric density, H is the scale height ($\sim$ 7 km), ϕ is the latitude, and z is the pressure height. The vertical integration is along a line of constant angular momentum, $\overline{m} = a\cos\phi\,(\overline{u} + a\Omega\cos\phi)$; dz' is the vertical projection of a segment of the $\overline{m}$. The relationship in the downward control principle expresses the fact that the interaction between the waves and mean flow is the driving force behind the mean meridional circulation, and this is in turn related to the non-acceleration theorem.

The adjustment time for the wave-mean flow interactions is several weeks in the lower stratosphere (Haynes et al. 1991), and thus it is possible to apply the downward control calculation to estimate the mean-meridional circulation by considering sufficiently long time averages (Rosenlof and Holton 1993). The downward control calculation was performed in z-coordinates, and then the analysis results were converted into isentropic coordinates using zonal mean geopotential height and potential temperature fields.

By using a zonal mean mass continuity equation, the mean meridional wind velocity is estimated as

$$\overline{v^*} = -\frac{1}{\rho_0 \cos\phi}\frac{\partial\psi}{\partial z}. \tag{3}$$

To estimate the relative contributions of the wave phenomena on various scales driving the mean-meridional circulation, the E-P flux is separated into three groups: planetary waves (PW), medium-scale waves (MW), and gravity waves (GW). The PW group is defined as the zonal wavenumber (s) components 1-3 using Fast Fourier Transformation (FFT). The MW group is defined as the total horizontal wavenumber (n) components 1-20, excluding the s = 1-3 components, which are extracted with a spherical filter using the Legendre transformation. The MW group includes synoptic-scale waves and sub-synoptic (medium)-

scale waves. The GW group is mostly composed of gravity waves, which are extracted with a spherical high-pass filter. The horizontal wavelengths of the GW group are between 188 km and 1900 km; these are not represented by most climate models (i.e., low-resolution GCMs). Watanabe et al. (2008) confirmed that the high-vertical-resolution GCM can resolve atmospheric waves with horizontal wavelengths of at least 210 km. It should be noted that the GW group includes both gravity waves and sub-synoptic-scale eddies.

2) Diffusion coefficients

We can characterize atmospheric mixing processes by estimating the diffusion coefficient using the eddy PV flux. By assuming a flux-gradient linear relationship, the diffusion coefficient provides a good measure of atmospheric mixing. The meridional diffusion coefficient in isentropic coordinates (K_{yy}) can be derived from the eddy meridional flux and meridional gradient of PV on isentropic surfaces (Tung, 1986; Bartels et. al., 1998; Newman et al., 1988; Miyazaki and Iwasaki, 2005):

$$\left[\overline{(v'q')^*}\right]_t \simeq -K_{yy}(t)\left[\left(\frac{\partial\overline{q^*}}{a\partial\phi}\right)_\theta\right]_t \tag{4}$$

where q is the PV, v is the meridional wind, θ is the potential temperature, and $[]_t$ denote the time average. The asterisks and overbars represent mass-weighting and isentropic zonal means, respectively. We assume that the source and sink terms of the PV due to diabatic processes and slant diffusions ($= -K_{yz}(t)\left[\left(\frac{\partial\overline{q^*}}{\partial z}\right)_\theta\right]_t$) are negligible. Lyjak and Yudin (2005) demonstrated that the diagnostic results for eddy mixing estimated from Kyy agree well with those estimated from the equivalent mixing length (whose square value is proportional to the effective diffusivity (Nakamura, 1996)) in the extratropical UTLS. Miyazaki and Iwasaki

(2009) also noted that most of the mixing properties are the same for the Kyy estimated from the PV and that estimated from long-lived tracers in the extratropical UTLS. This commonality suggests that the PV can be used as a tracer to diagnose atmospheric mixing. In addition, Miyazaki et al. (2009) confirmed that the diabatic source/sink effect on the PV budget is much less significant than transport effects in the extratropical UTLS. Therefore, the analysis results calculated with the eddy PV flux can be used to investigate atmospheric transport characteristics in these regions.

Steady conservative wave motions projected onto a meridional plane cause apparent diffusion in addition to the true diffusion caused by dissipative wave motions in Kyy (Miyazaki and Iwasaki, 2005). To remove the apparent diffusion effect caused by conservative wave motions and represent the Kyy caused by the true mixing, similar to the effective diffusivity, a time average window t can be applied to the eddy PV flux. Time averaged eddy PV flux fields act to reduce the effect of the apparent diffusion on Kyy. t is set to 1 day based on several sensitivity calculations. By increasing t to longer than 1 day, Kyy became only slightly smaller, but its spatial structure was somewhat noisier because of the smaller number of averaged samples (figure not shown).

A vertical diffusion coefficient derived from a flux-gradient relationship with the eddy vertical PV flux may not provide a good measure of atmospheric mixing. This is because variations in static stability lead to a non-linearity in the flux-gradient relationship. Instead, we can measure the strength of the vertical mixing from the vertical (diabatic) component of the eddy PV flux normalized by a background PV value;

$$\left| \frac{\overline{Q'q'}}{\overline{q}} \right| \tag{5}$$

where Q is the diabatic heating rate that leads to vertical air movements in isentropic coordinates. Thus, the vertical (diabatic) component of the eddy flux represents the strength of the vertical dispersions that deviate from isentropic surfaces through eddy motions. The eddy vertical PV flux increases as the PV increases with height. To measure the vertical mixing strength independent of the PV value, the eddy vertical PV flux is normalized using the background PV value. If the eddy vertical PV flux is sufficiently large compared to the background PV value, the vertical diffusion coefficient becomes large.

3. Mean-meridional circulation in the extratropical tropopause region

a. Each wave group's E-P flux

[Figure 1 about here.]

Figures 1a-c show the E-P flux and its divergence for each of the three wave groups for January, together with the 2 and 4 PVU (1 PVU = $10^{-6} Km^2 kg^{-1} s^{-1}$) surfaces; these PVU surfaces approximately correspond to the dynamical tropopause in the extratropics. Although the 2 PVU surface has widely been used to define the dynamical tropopause, it has been known to lie close to the bottom of the ExTL (e.g., Hoor et al., 2004) rather than the thermal tropopause (defined by the lapse rate profile following WMO (1957)). Miyazaki et al. (2009) showed that the 4 PVU surface is closer to the thermal tropopause than the 2 PVU surface in the high-resolution GCM.

Both the PW and MW E-P fluxes propagate upward in the troposphere and strongly converge in the upper troposphere and around the tropopause in the extratropics. The convergence of these E-P fluxes decelerates westerly wind. The convergence is stronger in the winter hemisphere than in the summer hemisphere. In the extratropical tropopause region, especially below θ=325 K, the PW E-P flux converges more obviously than the MW E-P flux. From the subtropics to mid-latitudes (latitudes of about 30°-40°), both the PW and MW E-P fluxes diverge in the lowermost stratosphere.

In contrast to the PW and MW E-P fluxes, the GW E-P flux diverges around and just above the tropopause from the subtropics to high latitudes, accelerating the westerly wind. This acceleration is commonly seen in both hemispheres. The strongest GW E-P flux divergence centers on the 40°-60° latitudes near the tropopause. The GW EP-flux divergence in the extratropical tropopause region may be affected by the spontaneous generation of inertia-gravity waves from jets and fronts. O'Sullivan and Dunkerton (1995) revealed the excitation and propagation of gravity waves near the tropopause related to baroclinic waves. Plougonven and Snyder (2007) also indicated a strong gravity wave packet in the tropopause region in the baroclinic life cycle dominated by cyclonic behavior.

The PW E-P flux obviously converges in the extratropical overworld stratosphere. The breaking of PWs leads to a strong deceleration of the westerly wind. This explains most of the deceleration by the total wave components. In the subtropical stratosphere, the convergence of the GW E-P flux largely influences the zonal mean zonal wind. This is more substantial in the winter hemisphere than in the summer hemisphere.

b. Wave-driven mean-meridional circulation

The downward control calculation using the E-P flux demonstrates that the PW group explains most of the forcing that drives the mean meridional circulation in the extratropical tropopause region and stratosphere (Figs. 1d-f). The convergence of the PW E-P flux drives a poleward-downward Brewer-Dobson circulation in the extratropical stratosphere and a fast mean poleward flow near and just below the extratropical tropopause. These velocities are much larger in the winter hemisphere than in the summer hemisphere. The MW group also induces a poleward and downward circulation in the extratropical upper troposphere. These facts have been commonly suggested by previous studies using coarse resolution GCMs (e.g., Rosenlof and Holton, 1993).

An analysis of the high-resolution GCM shows that the GW group causes a mean equatorward flow in the extratropical tropopause region (latitudes of 25°-70°, below approximately $\theta = 350$ K), which is associated with its E-P flux divergence. This differs from the mean poleward flow induced by the PW and MW groups. The mean equatorward flow induced by the GW group tends to partly cancel the mean poleward flow induced by the PW and MW groups.

The GW group also drives a mean poleward flow in the subtropical lower stratosphere (above approximately $\theta = 350$ K) and a mean downward flow in the mid-latitude lower stratosphere (latitudes of about 40°-50°). These flows are stronger in the winter hemisphere than in the summer hemisphere, corresponding to an interhemispheric difference in the GW E-P flux convergence. The poleward and downward circulation acts to transport air from the subtropical stratosphere to the mid-latitude tropopause region.

It should be noted that, in addition to the E-P flux divergence, the time tendency of the zonal mean zonal wind influences the mean-meridional circulation in the downward control calculation. However, this is not included in the analysis (Eq. (1)), which causes some disagreements in the mean meridional circulation between the total wave components downward control calculation and the residual mean-meridional circulation around the subtropical jet core.

4. Mixing processes in the extratropical tropopause region

a. Analysis of diffusion coefficients

1) Meridional structure in isentropic coordinates

[Figure 2 about here.]

Figure 2 depicts the meridional cross-section of the Kyy derived from the eddy PV flux for January and July in isentropic coordinates. The Kyy exhibits a complicated fine structure in the extratropical UTLS, with a minimum value centered on the subtropical jet stream. Large Kyy values in the extratropical tropopause region reveal obvious isentropic mixing across the tropopause below approximately $\theta = 340$ K during winter at the poleward-side of the subtropical jet stream. Active cross-tropopause mixing below $\theta = 340$ K has been commonly revealed by Lagrangian trajectory calculations (Berthet et al., 2007) and the relationships between different chemical species obtained from satellite measurements (Hegglin et al.,

2009). The average level of 340-350 K for the ExTL top found by Hegglin et al. (2009) suggests that the troposphere-to-stratosphere transport (i.e., mixing) is very active below this level. Birner (2006) evaluated the approximated observed PV structure of the TIL and found weak PV gradients confined to the TIL; these are suggestive of active large-scale dynamical mixing within the TIL. These observational analyses also appear to fit the high-vertical-resolution GCM analysis.

In the stratosphere ($\theta > 380$ K, i.e., the overworld stratosphere) of the winter hemisphere, the strong isentropic mixing revealed by the large Kyy values coincides with weak westerly wind. In comparison to that in the stratosphere, the Kyy is smaller in the lowermost stratosphere (between approximately $\theta = 330$ K and 380 K), implying less breaking of atmospheric waves in the middleworld stratosphere. The Kyy is smaller in the summer hemisphere than in the winter hemisphere throughout the extratropical UTLS. A very small Kyy value is observed over the Antarctic throughout the stratosphere in all seasons.

The Kyy is very small around the subtropical jet core between approximately $\theta = 330$ K and 390 K, where the atmospheric waves break less likely because of very strong westerly winds. The weak mixing suppresses the air exchange between the tropical upper troposphere and the extratropical lower stratosphere across the subtropical tropopause. The Kyy around the subtropical jet core is much smaller in the winter hemisphere than in the summer hemisphere, corresponding to a seasonal difference in zonal mean westerly wind speed as wel as monsoon circulation activity in the northern hemisphere. The stronger isentropic mixing around the subtropical tropopause is considered to make the chemical character of the extratropical lowermost stratosphere more tropospheric during summer than in other seasons (e.g., Hoor et al., 2004). A locally enhanced meridional PV gradient at the jet core may also

inhibit Rossby wave breaking and cause minima in Kyy in the jet (Hitchman and Huesmann, 2007). The Kyy is larger just below the subtropical jet stream than around the jet core.

These general characteristics of isentropic mixing derived from the Kyy using the high-resolution GCM output have been commonly revealed by Kyy estimates (Newman et al., 1988; Bratseth, 1998) and the effective diffusivity (Haynes and Shuckburgh, 2000) using the output of coarse-resolution models. The analysis of the high-vertical-resolution GCM indicates a larger maximum value and larger vertical variations of Kyy around the extratropical tropopause than that of coarse-resolution models.

Vertical mixing on the other hand is enhanced in the extratropical tropopause region at the mid-latitudes (latitudes of approximately 30°-60°), with larger values and areas in the summer hemisphere than in the winter hemisphere (Figs. 2c and 2d). Large vertical diffusion coefficient values are located between approximately 1 PVU and 8 PVU. This region is almost collocated with a mixing layer associated with stirring and mixing in the tropopause region identified from aircraft observations of ozone and carbon monoxide concentrations (Brioude et al., 2008). Hegllin et al. (2005) suggested that mixing across isentropes (i.e., vertical mixing) is more important than isentropic mixing in transporting chemical constituents in the lowermost stratosphere. In contrast, a very small vertical diffusion coefficient value is present just above the mixing layer. This small value suggests the existence of a vertical mixing barrier between the ExTL and higher levels. This vertical mixing barrier is associated with a very weak diabatic heating/cooling rate at this level, as a consequence of the cancellation between the short-wave heating by ozone and long-wave cooling by water vapor (c.f., Fig. 14b in Miyazaki et al. (2009)).

2) Meridional structure in tropopause-based coordinates

[Figure 3 about here.]

Figure 3 shows the diffusion coefficients in tropopause-based coordinates. The tropopause-based coordinates exhibit a more compact structure for the mixing layer relative to the tropopause, as compared to the standard coordinates in which the time average is taken at a constant height (or pressure) level. We first analyzed the Kyy in isentropic coordinates, and then converted it into tropopause-based coordinates. In other words, the temporal average of the analyzed Kyy was taken at a constant distance with respect to the zonal mean tropopause height (determined by the isentropic zonal mean temperature profile). Although this calculation method does not appropriately reflect local atmospheric structures related to longitudinal tropopause variations, it is still useful for demonstrating meridional transport processes in association with the mean tropopause location. On the other hand, the Kyy analyzed directly in standard tropopause-based coordinates (where the zonal average is taken at a constant distance with respect to the local tropopause height) cannot be physically interpreted (i.e., Kyy does not represent mixing by adiabatic wave motions, see also discussions in Miyazaki et al. (2009)).

The Kyy is large between approximately $\Delta\theta_{TP}$ = -20 K (-2.5 km) and +10 K (+1 km) throughout the extratropics of the winter hemisphere. Vertical mixing is very active at the mid-latitudes around the tropopause above approximately $\Delta\theta_{TP}$ = -20 K, especially in the summer hemisphere, but is substantially suppressed at $\Delta\theta_{TP}$ = +10 K to +15 K throughout the extratropics. Consequently, both the isentropic and vertical components of the eddy motions strongly diffuse air within the extratropical tropopause region between

approximately $\Delta\theta_{TP}$ = -20 K and +10 K.

The thickness of the simulated mixing layer is very consistent with that of the observed ExTL. Hegglin et al. (2009) identified an annual mean thickness of the ExTL to be approximately about 3 km in the NH extratropics, using satellite observations of chemical species and their correlations. Hoor et al. (2004) found an ExTL depth of about 20-25 K in winter and 30 K in summer. The similarity in the depths of the simulated mixing layer and observed ExTL implies that the mixing processes have considerable influences upon the location and depth of the ExTL. It should be noted that mean downward motions, together with mixing processes, distinctly affect chemical tracer concentration gradients (i.e., depth and seasonality of the ExTL) especially at the lower part of the ExTL (Miyazaki et al., 2009).

3) Seasonal variation in tropopause-based coordinates

[Figure 4 about here.]

[Figure 5 about here.]

The diffusion coefficients in tropopause-based coordinates show clear seasonal variations in the extratropical UTLS, as depicted in Figures 4 and 5. A large Kyy value is observed in the extratropical tropopause region throughout the year between approximately $\Delta\theta_{TP}$ = -20 K and + 10 K at 60 N, with a maximum in December and a minimum in August (Fig. 4a). The thickness of the layer with strong isentropic mixing is larger during winter than during summer. The upper boundary level of the mixing layer remains almost constant throughout the year, whereas the lower boundary level is about 10 K lower in winter

than in summer. A large Kyy at the tropopause level indicates strong mixing between the upper troposphere and lowermost stratosphere along isentropes. Strong isentropic mixing at the tropopause level is present at latitudes of approximately 40°-80° in both hemispheres, reaching a maximum at around 50 N and 60 S in mid-winter (Fig 5a). The seasonal and latitudinal variations in Kyy at the tropopause level appear to correspond well with those in baroclinic wave activity, implying that baroclinic waves act to effectively flatten chemical tracer concentration gradients along isentropes at the tropopause level at these latitudes.

In the overworld stratosphere (above $\Delta\theta_{TP} = +60$ K) at 60 N, the Kyy is large from November to February and very small from June to September (Fig. 4a). Compared to that in the overworld stratosphere, the Kyy has less seasonality in the middleworld stratosphere (between approximately $\Delta\theta_{TP} = +30$ K and +60 K). The Kyy and zonal mean zonal wind show similar seasonal variations in the stratosphere.

Vertical mixing in the extratropical tropopause region is very strong from June to August and is weak from November to March at 60 N (Fig. 4b). This seasonal variation is very different from that of isentropic mixing. Strong vertical mixing across the tropopause occurs at latitudes of 40°-65° during summer in both hemispheres (Fig. 5b). The summertime active vertical mixing at mid latitudes may be strongly associated with three-dimensional turbulence and convection. It appears that the active vertical mixing results in smaller CO concentration gradients across the tropopause during summer than in other seasons (Hoor et al., 2004; Hegglin et al., 2009). In contrast, the vertical mixing suppression related to a very weak diabatic heating rate persists throughout the year at around $\Delta\theta_{TP} = +10$ K to +20 K.

Around the subtropical tropopause, both the Kyy and zonal mean zonal wind show

obvious seasonal variations (Fig. 4c). A small Kyy is related to a strong westerly wind from November to April, where atmospheric waves do not break easily. In contrast, from June to August, the Kyy is large between approximately $\Delta\theta_{TP}$ = -20 K to +40 K, allowing mixing between the tropical upper troposphere and extratropical lower stratosphere, as consistently reported by observational study (e.g., Hoor et al., 2004). The strong isentropic mixing extends across the latitudes of 15°-35° (Fig. 5a).

b. Implication from 2-D model simulations

[Figure 6 about here.]

In Section 4.1, we demonstrated the characteristics of the mixing processes. Here, in this section, we briefly demonstrate the roles of these mixing processes in determining the PV (or constituent) distributions. For this purpose, we compare the PV distributions of the GCM simulation and the integration results of a zonal mean PV continuity equation based on mass-weighted isentropic zonal means (MIM) analysis (Miyazaki et al. (2009); i.e., a two-dimensional (2-D) model simulation):

$$\frac{\partial \overline{q^*}}{\partial t} = -\frac{\overline{v^*}}{a}\frac{\partial \overline{q^*}}{\partial \phi} - \overline{\dot{\theta}^*}\frac{\partial \overline{q^*}}{\partial \theta} - \frac{1}{a\cos\phi}\frac{\partial \overline{(v'q')^*\cos\phi}}{\partial \phi} - \frac{1}{\rho_0}\frac{\partial \rho_0 \overline{(\dot{\theta}'q')^*}}{\partial z_\dagger} + \overline{\left(q\frac{\partial \dot{\theta}}{\partial \theta}\right)^*}, \qquad (6)$$

The first term on the right hand side of Eq. (6) represents the PV time tendency due to mean meridional transport the second term is that due to mean vertical transport, the third term is that due to eddy meridional transport, the fourth term is that due to eddy vertical transport, and the fifth term is that due to source/sink related to changes in stability through diabatic processes. Although the PV structure is associated strongly with the atmospheric

stability profile, its temporal evolution is caused by atmospheric transport processes together with diabatic source/sink effects. By excluding the eddy transport terms in the zonal mean equation and comparing the simulation result with the GCM simulation, we show the effects of the mixing processes.

In a standard 2-D model simulation, we neglected the influence of the eddy meridional and vertical transport terms in the zonal mean equation (Eq. (6)), but considered the PV tendencies using the mean transport and non-conservative (diabatic source/sink) terms. A comparison between this 2-D model simulation and the GCM simulation result demonstrates the importance of the eddy transport. In addition, another 2-D model simulation was performed that considered the eddy vertical transport term together with the mean transport and non-conservative terms (i.e., only the eddy meridional transport term was neglected), demonstrating the importance of isentropic mixing on PV distributions. The mean-meridional circulation fields and static stability profiles obtained from the GCM simulation results were provided for the 2-D model simulation to calculate the mean transport and non-conservative terms. Twenty day integrations were performed starting at January 1st and at July 1st, using the initial PV distributions obtained from the GCM simulation results.

Figure 6 compares the zonal mean PV profiles between the GCM and 2-D model simulations averaged between 50 N-60 N, for January 14th-20th and July 14th-20th. The 2-D model that neglected both the eddy meridional and vertical transport terms has a larger PV value around the tropopause and a much smaller vertical PV gradient just above the tropopause compared to the GCM during winter. As a result of excluding the eddy transport terms, the maximum PV gradient height falls to about 10 K near the tropopause. The lower

height of the maximum gradient is commonly revealed by another 2-D model simulation that includes the eddy vertical transport. The active isentropic mixing identified from a large Kyy strongly diffuses air within the extratropical tropopause region between approximately θ_{TP} = -20 K and +10 K, lifting the maximum PV gradient from just below to just above the tropopause. This effect makes an important contribution to the formation of large tracer gradients in the upper part of the ExTL.

During summer, the maximum PV gradient simulated using the GCM is located near $\Delta\theta_{TP}$ = +5 K. The 2-D model that neglects both the eddy meridional and vertical transport terms indicates a lower height for the maximum PV gradient around the tropopause. By including the eddy vertical transport term, the maximum PV gradient height and PV profile in the 2-D model simulation approach those in the GCM just above the tropopause. Very strong vertical mixing occurs between approximately θ_{TP} = -20 K and +10 K at the NH mid latitudes during summer. Variations in vertical mixing (i.e., convergence of eddy vertical fluxes) act to shift the vertical PV gradient from around to just above the tropopause. The results imply that vertical mixing is more important for determining the height of the large PV (or constituent) gradient around the tropopause during summer than during winter, in association with the strong convergence of eddy vertical fluxes at just above the tropopause (i.e., vertical mixing barrier).

c. Wave characteristics: Isentropic mixing

1) Vertical profile

[Figure 7 about here.]

[Figure 8 about here.]

In order to investigate the relative contributions of atmospheric motions with different horizontal-scales to isentropic mixing, the eddy PV flux can be decomposed into individual zonal wavenumber components using FFT. The eddy PV fluxes at the different zonal wavenumbers (s) normalized by the background PV gradient measure the contributions of the different horizontal-scale atmospheric disturbances to the total Kyy:

$$K_{yy(s)} = \left(\frac{\left| \overline{v'_s q'_s} \right|}{\frac{\partial \overline{q^*}}{a \partial \phi}} \right)_\theta \tag{7}$$

Figures 7 and 8 depict the zonal wavenumber dependence of the normalized isentropic eddy PV flux averaged between 50 N and 60 N (where mixing in both the isentropic and vertical directions are very strong around the tropopause) in January. The isentropic eddy PV flux is strongly influenced by large and medium horizontal-scale motions, particularly those with $s \leq$ 12-13 below $\theta = 325$ K and $s \leq$ 5-6 above the level. In other words, planetary waves largely contribute to isentropic mixing in the stratosphere, while both planetary-scale and synoptic-scale waves cause strong isentropic mixing below the lowermost stratosphere. Medium-scale waves with horizontal wavelengths of a few thousand km (Sato et al., 1993) also seem to contribute to the isentropic mixing below the lowermost stratosphere. Small Kyy values in the middleworld stratosphere (c.f., Fig. 2a) mostly arise from small contributions by large horizontal-scale motions, especially around $\theta =$ 370-400 K.

It is worth noting that atmospheric motions with horizontal wavelengths of less than a few thousand kilometers play essential roles in isentropic mixing just above the extratropical tropopause (as seen in Fig. 8b). These small horizontal-scale motions (i.e., $s \geq 21$) cause stronger isentropic mixing between $\theta = 330$ K and 355 K than at other levels in the

stratosphere. Both the small horizontal-scale motions and static stability are maximized at around 340-350 K (Fig. 7), suggesting that active isentropic mixing is connected with rapid changes in the static stability through small-scale dynamics around the TIL.

Figure 8 compares the relative contribution of each wave group to the total isentropic mixing at the NH mid-latitudes in January. The small horizontal-scale motions (i.e., $s \geq 21$) provide an important contribution to the total isentropic mixing just above the tropopause, with a contribution of about 20 %. Although large horizontal-scale motions dominate the strength of the isentropic mixing in the extratropical UTLS (the contribution of planetary wave-scale motions (i.e., $s \leq 3$) is more than 30 % in the troposphere and reaches 45 % at 450 K), the enhanced contribution of the small horizontal-scale mixing is a unique and important characteristic of the extratropical tropopause region.

2) Seasonal and interhemisperic differences

[Figure 9 about here.]

The dominant horizontal-scales appearing in the isentropic mixing differ somewhat between the two hemispheres and different seasons in the extratropical UTLS, as depicted in Figure 9. At the NH mid-latitudes during summer, large horizontal-scale mixing is the strongest just below the tropopause and weakens rapidly with height in the stratosphere (Fig. 9a), which is different from winter. In particular, large horizontal-scale mixing, with s = 1-4, makes a much weaker contribution to the total isentropic mixing in the stratosphere during summer than during winter. The seasonal variation in the planetary wave activity dominates that of the Kyy in the NH stratosphere.

Isentropic mixing, with s = 1-2, is much weaker in the SH than in the NH during winter (Fig. 9b). Quasi-stationary planetary wave activity is weaker in the SH than in the NH. This is responsible for the weaker large-scale mixing in the SH. In contrast, synoptic-scale mixing, with s = 4-7, is somewhat stronger in the SH than in the NH in the upper troposphere and around the tropopause, which is attributable to the interhemispheric difference in baroclinic wave activity.

Small horizontal-scale mixing just above the extratropical tropopause is stronger in winter than in summer, and in the NH than in the SH. In the SH, small horizontal-scale mixing is strongest just below the tropopause, just as in the NH, but rapidly weakens with height in the lower stratosphere, which is different from the NH (Fig. 9b).

In the subtropical UTLS during summer, isentropic mixing is dominated by large horizontal-scale mixing, with s = 1-7 (Fig. 9c). This suggests that the active cross-tropopause mixing is attributable to Rossby wave breaking in the subtropics during summer, as commonly suggested by Postel and Hitchman (1999). Small horizontal-scale mixing reaches a maximum in the lower stratosphere between 390 K and 420 K in the subtropics, collocating with the strong GW E-P flux convergence (c.f., Fig. 1c).

3) Wave characteristics: Vertical mixing

[Figure 10 about here.]

[Figure 11 about here.]

Here we consider the occurrence of vertical mixing due to diabatic processes around the TIL. The vertical mixing processes around the TIL seem to obviously change the vertical

gradients of the chemical constituent concentrations around the ExTL. In order to review the vertical mixing characteristics in the TIL, Figure 11 shows the vertical profile of the eddy vertical PV flux normalized by the background PV value for each zonal wavenumber (which is proportional to the vertical diffusion coefficient (Eq. (5)):

$$\left| \frac{\overline{Q'_s q'_s}}{\overline{q}} \right| \tag{8}$$

The vertical dispersion by small-scale eddy motions with horizontal wavelengths of less than a few thousand km is clearly strengthened just above the tropopause between approximately $\theta = 330$ K and 360 K (Fig. 11), while that by large-scale eddy motions is weaker at this level compared to those at other levels. Small horizontal-scale motions, with $s \geq 21$, provide dominant contributions to the total vertical mixing in the lower stratosphere below 400 K (Fig. 12), reaching a maximum between 345 K and 375 K.

As a result, small horizontal-scale motions lead to strong eddy PV fluxes in both the isentropic and vertical directions just above the tropopause (c.f., Figs. 8 and 12). The analysis results confirm the occurrence of obvious three-dimensional mixing by small-scale motions around the TIL. It should be noted that isentropic coordinates might not be suitable for representing vertical mixing related to overturning isentropes involved in breaking gravity wave.

4) Spatial distribution

[Figure 12 about here.]

Figure 12a shows the spatial distribution of the monthly-mean amplitude of small horizontal-

scale PV disturbances for $s \geq 21$ on the 360 K surface (located just above the tropopause in the extratropics (i.e., in the TIL) but in the upper troposphere in the tropics). The small horizontal-scale PV disturbances, probably strongly associated with small-scale variability in N_2, are large over strong convection regions (i.e., the maritime continental region), mountainous regions (i.e., over the Rocky Mountains, Himalayas, Iceland, and Antarctic Peninsula), and the polar sides of the subtropical westerly jet stream. A snap shot picture (Fig. 12b) clearly exhibits the horizontal structures (including the lateral propagations) of the small horizontal-scale PV disturbance over strong convective regions (e.g., the southeast Asian maritime continent), frontal systems (e.g., in the SH east Pacific), and mountainous regions. These small-scale disturbances occur over possible sources of gravity waves (i.e., high mountains, cyclones, fronts, and convection), suggesting that the propagation and breaking of gravity waves lead to active small-scale mixing in the TIL. Three-dimensional gravity wave propagation in the high-resolution GCM is further discussed in Watanabe et al. (2008) and Sato et al. (2009).

5. Discussions: Small-scale mixing around the TIL

[Figure 13 about here.]

[Figure 14 about here.]

In this section, we discuss possible mechanisms for the three-dimensional mixing processes (i.e., isentropic and vertical mixing) in the TIL associated with atmospheric waves. Hegglin et al. (2009) discussed that Rossby wave breaking events cause filaments of tro-

pospheric air advected into the lowermost stratosphere, and that these filaments may be three-dimensionally mixed by small-scale motions, i.e., turbulence generated by dynamical processes such as gravity waves. Gravity wave dissipation occurs when the waves break or encounter critical levels. Meanwhile, even if gravity waves do not break or encounter critical levels, large-amplitude gravity waves can have eddy vertical dispersions and induce net three-dimensional mixing under non-uniform diabatic heating rate fields. In other words, zonal variations in the diabatic heating rate on wave (or isentropic) surfaces generate the eddy components of the vertical dispersions away from the surfaces.

First, we investigate the gravity wave energy around the TIL. Figure 13 depicts the potential energy ($PE = \frac{1}{2}\frac{g^2}{N^2}\frac{\overline{\theta'^2}}{\overline{\theta}^2}$) and kinetic energy ($KE = \frac{1}{2}\left(\overline{u'^2} + \overline{v'^2} + \overline{w'^2}\right)$) of gravity waves in January. Small horizontal-scale fluctuations with total wavenumbers (n) greater than 22 are analyzed as gravity waves, although filamentary structures also contribute to the small-scale fluctuations around the tropopause (figure not shown). The large total energy of the gravity waves (TE = KE + PE) is observed from the upper troposphere to just above the tropopause in the extratropics, which is mostly attributable to KE. A local maximum PE also contributes to the large TE just above the tropopause. As a result, the relative ratio of PE to KE (PE/KE, Fig. 13d) is maximized in the middle troposphere and just above the tropopause and is minimized just below the tropopause. A local maximum for the relative ratio lying just above the tropopause coincides with the N^2 maximum. The enhancement of gravity wave energy near the tropopause has been commonly investigated by radiosonde and GPS radio occultation data (e.g., Allen and Vincent, 1995; Schmidt et al., 2008), and is considered to be an important characteristic of the extratropical tropopause region.

Second, we consider the dissipation and saturation of the gravity waves around the TIL.

Following the linear wave theory (e.g., Lindzen, 1981), the breaking level of gravity waves is defined as the level where the isentrope first becomes $\frac{\partial \theta}{\partial z} = \frac{\partial \overline{\theta}}{\partial z} + \frac{\partial \theta'}{\partial z} = 0$. The assumption in this theory is that any wave amplitude in excess of the threshold value causes instability and turbulence and acts to prevent further growth of the wave amplitude (i.e., the waves become convectively unstable). In the TIL, the zonal mean static stability is large, making the gravity wave saturation amplitude large. The large-amplitude gravity waves can cause vertical eddy dispersions owing to non-uniform diabatic fields. In addition, the large-amplitude gravity waves may be easily dissipated due to radiative relaxation. In contrast, in the upper part of and just above the TIL, as the static stability decreases with height (and the gravity wave amplitude increases with height because of the exponential decrease of atmospheric density), gravity waves may easily reach their saturation limit and breaking level and cause three-dimensional turbulence and mixing.

Meanwhile, dynamical instability plays a significant role in the saturation of gravity waves. Gravity wave saturation is significant in the enhancement of momentum flux deposition and turbulent diffusion (e.g., Dunkerton, 1989). The dynamical instability occurs in the presence of a vertical mean wind shear (e.g., around the tropopause owing to the presence of a jet stream). In order to measure the stability of the gravity waves, we can estimate the probability of the occurrence of the dynamical instability based on the Richardson number (Ri):

$$Ri = \frac{N^2}{\left(\frac{\partial \overline{u}}{\partial z}\right)^2} \tag{9}$$

The atmosphere is dynamically unstable when $Ri < 0.25$. Figure 14 shows that this dynamical instability occurs more frequently in the extratropical tropopause region between

approximately $\Delta\theta_{TP}$ = -10 K and +30 K, compared to other levels, where large amplitude inertia-gravity waves may undergo breaking. The region of large dynamical instability almost corresponds to the strong small-scale three-dimensional mixing region (c.f., Section 4).

Consequently, these small-scale dynamics in association with the dissipation and saturation of gravity waves seem to explain the obvious three-dimensional mixing by small-scale motions around the TIL, and might be the essential cause of the large constituent concentration gradients around the ExTL. However, further study is still required to the comprehend gravity wave processes related to the rapid change in the static stability around the TIL (e.g., generation mechanisms, changes in vertical wavelength).

6. Conclusions

[Figure 15 about here.]

The roles of atmospheric processes with various scales, including gravity wave-scale to planetary-scale phenomena, in the transport and mixing processes in the extratropical tropopause were examined using a high-vertical-resolution GCM. The GCM has a vertical resolution of about 300 m above the extratropical upper troposphere and represents the dynamic and thermal fine-scale structure of the extratropical tropopause region. The GCM made it possible to resolve most of the gravity waves and represent their propagation and breaking in the lower and middle atmosphere. Our analysis of atmospheric processes with different scales provides a comprehensive view of transport and mixing in the extratropical tropopause region (Figure 15). The dominant transport scale differs between the tropopause

region and other levels in the UTLS.

The relative contributions of atmospheric waves with different scales, including resolved gravity waves, to the driving of the mean meridional circulation have been examined using the downward control calculation. The E-P flux associated with gravity waves diverges and induces a mean equatorward flow in the extratropical tropopause region. The mean equatorward flow induced by the gravity wave E-P flux divergence partly cancels a mean poleward flow induced by the planetary and synoptic-scale wave E-P flux convergence near the extratropical tropopause. The gravity waves also drive a mean poleward circulation in the subtropics and a mean downward circulation at the mid-latitudes in the lower stratosphere of the winter hemisphere.

The diffusion coefficients estimated from the eddy PV fluxes in tropopause-based coordinates were used to investigate the significance of the eddy transport in the extratropical tropopause region. The air within the extratropical tropopause region between approximately $\Delta\theta_{TP}$ = -20 K and +10 K was found to be strongly diffused due to adiabatic eddy motions from late autumn to early spring. Vertical eddy motions are substantial in the tropopause region at the mid-latitudes during summer, but are strongly suppressed at $\Delta\theta_{TP}$ = +10 to 15 K just above the well-mixed region throughout the year. The simulated mixing layer almost coincided with the observed ExTL, suggesting that mixing processes play important role in determining the depth and location of the ExTL. The Kyy was found to be very small around the subtropical westerly jet, inhibiting the transport of tropical tropospheric air into the extratropical lowermost stratosphere.

It should be emphasized that small-scale motions with horizontal wavelengths of less than a few thousand km were found to cause obvious three-dimensional mixing just above

the extratropical tropopause (i.e., in the TIL), as depicted in Fig. 15b. This small horizontal-scale mixing in the TIL is stronger during winter than during summer, and in the NH than in the SH. In contrast, large-scale waves cause strong isentropic mixing below the lowermost stratosphere. Small horizontal-scale disturbances are large over regions with possible sources of gravity waves (high mountains, cyclones, fronts, and convection) at the TIL level. The analysis of the gravity wave energy proved an enhancement of gravity wave PE just above the tropopause. The enhanced PE contributes to the increase in total gravity wave energy in the TIL, along with a large KE.

In the TIL, the saturation amplitude of the gravity waves can be large because of a large static stability. This situation allows the occurrence of large-amplitude gravity waves. Even when gravity waves do not break, large-amplitude gravity waves can be dissipated due to radiative relaxation and can cause eddy vertical dispersions under non-uniform diabatic heating rate fields. In contrast, in the upper part of and just above the TIL, gravity waves may easily reach their saturation limit and breaking level because of a decrease in static stability and atmospheric density with height. Dynamic instability occurs more frequently in the extratropical tropopause region than at other levels, which also may lead to the saturation of gravity waves. These situations associated with the dissipation and saturation of gravity waves seem to cause small-scale three-dimensional mixing around the TIL.

To summarize, the small-scale dynamics associated with the propagation and breaking of gravity waves play important roles in driving tracer transports by both the mean-meridional circulation and three-dimensional mixing in the extratropical tropopause region. It may be important to include these small-scale dynamic effects in GCMs or CTMs to obtain better simulations of the TIL and ExTL.

Acknowledgments.

The authors are grateful to S. Tateno for his help to make the analysis of gravity wave energy, and S. Ogino for his helpful discussions. We would also like to thank the anonymous reviewers and T. Birner for their valuable comments. This work is a contribution to the Innovative Program of Climate Change Projection for the 21st Century, MEXT, Japan. The work was partly supported by Grant-in Aid for Scientific Research 19204047 of MEXT, Japan and by a Japan Society for the Promotion of Science Grant-in-Aid for Young Scientists (B) 19740300. The calculation was conducted using the Earth Simulator.

REFERENCES

Allen, S. J. and R. A. Vincent, 1995: Gravity wave activity in the lower atmosphere: Seasonal and latitudinal variations. *J. Geophys, Res.*, **100**, 1327–1350.

Andrews, D. G., and M. E. McIntyre, 1976: Planetary waves in horizontal and vertical shear: The generalized Eliassen-Palm relation and mean-zonal acceleration. *J. Atmos. Sci.*, **33**, 2031–2048.

Bartels, J., D. Peters, G. Schmitz, 1998: Climatological Ertel's potential-vorticity flux and mean meridional circulation in the extratropical troposphere - lower stratosphere. *Ann Geophysicae*, **16**, 250-265.

Berthet, G., J. G. Esler, and P. H. Haynes, 2007: A Lagrangian perspective of the tropopause and the ventilation of the lowermost stratosphere. *J. Geophys. Res.*, **112**, D18102, doi:10.1029/2006JD008295.

Birner, T., A. Dornbrack, and U. Schumann, 2002: How sharp is the tropopause at midlatitudes? *Geophys. Res. Lett.*, **29**, 1700, doi:10.1029/2002GL015142.

Birner, T., 2006: Fine-scale structure of the extratropical tropopause region. *J. Geophys. Res.*, **111**, D04104, doi:10.1029/2005JD006301.

Bratseth A. M., 1998: On the estimation of transport characteristics of atmospheric data sets. *Tellus*, **50A**, 451–467.

Brioude, J., J.-P. Cammas, O. R. Cooper, and P. Nedelec, 2008: Characterization of the composition, structure, and seasonal variation of the mixing layer above the extratropical tropopause as revealed by MOZAIC measurements. *J. Geophys. Res.*, **113**, D00B01, doi:10.1029/2007JD009184.

Chen, P., Holton, J. R., O'Neill, A. and Swinbank, R, 1994: Isentropic mass exchange between the tropics and extratropics in the stratosphere. *J. Atmos. Sci.*, **51**, 3006–3018.

Clark T. L., and W. R. Peltier, R, 1977: On the evolution and stability of finite amplitude mountain waves. *J. Atmos. Sci.*, **34**, 1715–1730.

Duck, T. and J. A. Whiteway, 2005: The spectrum of waves and turbulence at the tropopause. *Geophys. Res. Lett.*, **32**, L07801.

Dunkerton, T. J., 1989: Theory of internal gravity wave saturation. *Pure and Appl. Geophys.*, **130**, 373–397.

Fischer, H., F. G. Wienhold, P. Hoor, O. Bujok, C. Schiller, P. Siegmund, M. Ambaum, H. A. Scheeren, and J. Lelieveld, 2000: Tracer correlations in the northern high latitude lowermost stratosphere: Influence of cross-tropopause mass exchange. *Geophys. Res. Lett.*, **27**, 97-100, doi:10.1029/1999GL010879.

Fritts, D.C. and Alexander, M. J,, 2003: Gravity wave dynamics and effects in the middle atmosphere. *Rev. Geophys.*, **41**, doi:10.1029/2001RG000106.

Haynes, P. H., Marks, C. J., McIntyre, M. E., Shepherd, T. G., Shine, K. P., 1991: On the "downward control" of extratropical diabatic circulations by eddy-induced mean zonal forces. *J. Atmos. Sci.*, **48**, 651–678.

Haynes, P. H., and E. F. Schuckburgh, 2000: Effective diffusivity as a diagnostic of atmospheric transport. 2. Troposphere and lower stratosphere. *J. Geophys. Res.*, **105**, 22795–22810.

Hegglin, M. I., D. Brunner, T. Peter, J. Staehelin, V. Wirth, P. Hoor, and H. Fischer, 2005: Determination of eddy diffusivity in the lowermost stratosphere, *Geophys. Res. Lett.*, **32**, L13812, doi:10.1029/2005GL022495.

Hegglin, M. I., C. D. Boone, G. L. Manney, and K. A. Walker, 2009: A global view of the extratropical tropopause transition layer from Atmospheric Chemistry Experiment Fourier Transform Spectrometer O3, H2O, and CO. *J. Geophys. Res.*, **114**, D00B11, doi:10.1029/2008JD009984.

Hitchman, M. H., and A. S. Huesmann, 2007: A seasonal climatology of Rossby wave breaking in the layer 330-2000 K. *J. Atmos. Sci.*, **39**, 1922–1940.

Holton, J. R., P. H. Haynes, M. E. McIntyre, A. R. Douglass, R. B. Rood, and L. Pfister, 1995: Stratosphere-troposphere exchange. *Rev. Geo- phys.*, **33**, 403–439.

Hoor, P., C. Gurk, D. Brunner, M. I. Hegglin, H. Wernli, and H. Fischer, 2004: Seasonality and extent of extratropical TST derived from in-situ CO measurements during SPURT. *Atmos. Chem. Phys.*, **4**, 1427–1442.

Lamarque, J.-F., Langford A., and M. Proffitt, 1996: Cross-tropopause mixing of ozone through gravity wave breaking: Observation and modeling. *J. Geophys. Res.*, **22**, 22969–22976.

Lane, T.P., R.D. Sharman, T.L. Clark, and H.-M. Hsu, 2003: An investigation of turbulence generation mechanisms above deep convection. *J. Atmos. Sci.*, **60**, 1297–1321.

Lane, T. P., and R. D. Sharman, 2008: Some influences of background flow conditions on the generation of turbulence due to gravity wave breaking above deep convection. *J. Appl. Met. Climatol.*, **47**, 2777–2796.

Lindzen, R. S., 1981: Turbulence and stress owing to gravity wave and tidal breakdown. *J. Geophys. Res.*, **86**, 9707–9714.

Lyjak, L. V., and V. A. Yudin, 2005: Diagnostics of the large-scale mixing properties from stratospheric analyses. *J. Geophys. Res.*, **110**, D17107, doi:10.1029/2004JD005577.

McIntyre, M. E., and T. N. Palmer, 1984: The "surf zone" in the stratosphere. *J. Atmos. Terr. Phys.*, **46**, 825–849.

Miyazaki, K., and T. Iwasaki, 2005: Diagnosis of meridional ozone transport based on mass weighted isentropic zonal means. *J. Atmos. Sci.*, **63**, 1192–1208.

Miyazaki, K., and T. Iwasaki, 2009: Isentropic diffusion coefficient derived from chemical constituent data. *Scientific Online Letters on the Atmosphere*, **5**, 009-012, doi:10.2151/sola.2009-003.

Miyazaki K., S. Watanabe, Y. Kawatani, Y. Tomikawa, K. Sato, and M. Takahashi, 2009: Transport and mixing in the extratropical tropopause region in a high vertical resolution GCM. Part I: Potential vorticity and heat budget analysis. *J. Atmos. Sci.*, revised.

Nakamura, N., 1996: Two-dimensional mixing, edge formation, and permeability diagnosed in area coordinates. *J. Atmos. Sci.*, **53**, 1524–1537.

Newman, P.A., M.R. Schoeberl, R.A. Plumb, and J.E. Rosenfield, 1988: Mixing rates calculated from potential vorticity. *J. Geophys. Res.*, **93**, 5221–5240.

O'Sullivan, D. J. and T. J. Dunkerton, 1995: Generation of inertia-gravity waves in a simulated lifecycle of baroclinic instability. *J. Atmos. Sci.*, **52**, 3695-3716.

Pavelin, E., Whiteway, J., Busen, R. and Hacker, J., 2002: Airborne observations of turbulence, mixing and gravity waves in the tropopause region. *J. Geophys. Res.*, **107**, 4084, doi:10.1029/2001JD000775.

Plougonven, R., and C. Snyder, 2005: Gravity waves excited by jets: Propagation versus generation. *Geophys. Res. Lett.*, **32**, L18802, doi:10.1029/2005GL023730.

Plougonven, R., and C. Snyder, 2007: Inertia-gravity waves spontaneously generated by jets and fronts. Part I: Different baroclinic life cycles. *J. Atmos. Sci.*, **64**, 2502–2520.

Postel, G. A. and M. H. Hitchman, 1999: A climatology of Rossby wave breaking along the subtropical tropopause. *J. Atmos. Sci.*, **56**, 359–373.

Postel, G. A. and M. H. Hitchman, 2001: A case study of Rossby wave breaking along the subtropical tropopause. *Mon. Wea. Rev.*, **129**, 2555-2569.

Rosenlof, K. H., and J. R. Holton, 1993: Estimates of the stratospheric residual circulation using the downward control principle. *J. Geophys. Res.*, **98**, 10,465-10,479.

Sato, K., 1994: A statistical study of the structure, saturation and sources of inertio-gravity waves in the lower stratosphere observed with the MU radar. *J. Atmos. Terr. Phys.*, **56**, 755–774.

Sato, K., D. J. O'Sullivan and T. J. Dunkerton, 1997: Low-frequency inertia-gravity waves in the stratosphere revealed by three-week continuous observation with the MU radar. *Geophys. Res. Lett.*, **24**, 1739–1742.

Sato, K., H. Eito, and I. Hirota, 1993: Medium-scale traveling waves in the extratropical upper troposphere. *J. Met. Soc. Japan*, **71**, 427–436.

Sato, K., S. Watanabe, Y. Kawatani, Y. Tomikawa, K. Miyazaki, and M. Takahashi, 2009: On the origins of mesospheric gravity waves. *Geophys. Res. Lett.*, **36**, L19801, doi:10.1029/2009GL039908.

Schmidt, T.; de la Torre, A.; Wickert, J, 2008: Global gravity wave activity in the tropopause region from CHAMP radio occultation data. *Geophys. Res. Lett.*, **35**, L16807, doi:10.1029/2008GL034986.

Shapiro, M. A., 1980: Turbulent mixing within tropopause folds as a mechanism for the exchange of chemical constituents between the stratosphere and troposphere. *J. Atmos. Sci.*, **37**, 994–1004.

Stone, E. M., W. J. Randel, and J. L. Stanford, 1999: Transport of passive tracers in baroclinic wave life cycles. *J. Atmos. Sci.*, **56**, 1364-1381.

Tomikawa, Y., K. Sato, S. Watanabe, Y. Kawatani, K. Miyazaki, and M. Takahashi, 2008:

Wintertime temperature maximum at the subtropical stratopause in a T213L256 GCM. *J. Geophys. Res.*, **113**, D17117, doi:10.1029/2008JD009786.

Tung K. K., 1986: Nongeostrophic theory of zonally averaged circulation. Part I: Formulation, *J. Atmos. Sci.*, **43**, 2600–2618.

VanZandt, T. E., and D. C. Fritts, 1989: A theory of enhanced saturation of the gravity wave spectrum due to increases in atmospheric stability. *Pure Appl. Geophys.*, **130**, 399–420.

Watanabe, S., Y. Kawatani, Y. Tomikawa, K. Miyazaki, M. Takahashi, and K. Sato, 2008: General aspects of a T213L256 middle atmosphere general circulation model. *J. Geophys. Res.*, **113**, D12110, doi:10.1029/2008JD010026.

Watanabe, S., Y. Kawatani, Y. Tomikawa, K. Miyazaki, M. Takahashi, and K. Sato, 2009: Simulation of the Eastward 4-day Wave in the Antarctic Winter Mesosphere Using a Gravity Wave Resolving General Circulation Model. *J. Geophys. Res.*, **114**, D16111, doi:10.1029/2008JD011636.

WMO, 1957: Definition of the tropopause. *WMO Bull.*, **6**, 136.

Yamamori, M., K. Sato, and I. Hirota, 1997: A study on seasonal variation of upper tropospheric medium-scale waves over East Asia based on regional climate model data. *J. Met. Soc. Japan*, **75**, 13–22.

List of Figures

4 Seasonal variation of (a, c) the logarithms of the isentropic diffusion coefficient (K_{yy}, in $m^2 s^{-1}$) and (b) the vertical diffusion coefficient ($\frac{\overline{Q'q'}}{\overline{q}}$, in Ks^{-1}) at (a, b) 60 N and (c) 30 N, as a function of the distance from the thermal tropopause ($\Delta\theta_{TP}$). The black contour lines represent the zonal mean zonal wind with intervals of 5 ms^{-1}. The white contour lines represent the absolute values of PVU at 2 and 4 PVU. 48

5 Seasonal variation of (a) the logarithms of the isentropic diffusion coefficient (K_{yy}, in $m^2 s^{-1}$) and (b) the vertical diffusion coefficient ($\frac{\overline{Q'q'}}{\overline{q}}$, in Ks^{-1}) at the thermal tropopause height ($\Delta\theta_{TP}$=0). The black contour lines represent zonal mean zonal wind with intervals of 10 ms^{-1}. 49

6 Vertical profiles of PV value (first column), vertical PV gradient (in $PVUkm^{-1}$, second column), and the logarithm of Kyy (in $m^2 s^{-1}$, third column) and the vertical diffusion coefficient ($\frac{\overline{Q'q'}}{\overline{q}}$, in Ks^{-1}, forth column), as functions of the distance from the thermal tropopause ($\Delta\theta_{TP}$) average between 50 N and 60 N, during (a) January 14th-20th and (b) July 14th-20th, obtained from the GCM simulation (solid line), the 2-D model calculation that neglected both the eddy meridional and vertical transport terms (dotted line), and the 2-D model calculation that only neglected the eddy meridional transport term (dashed line). 50

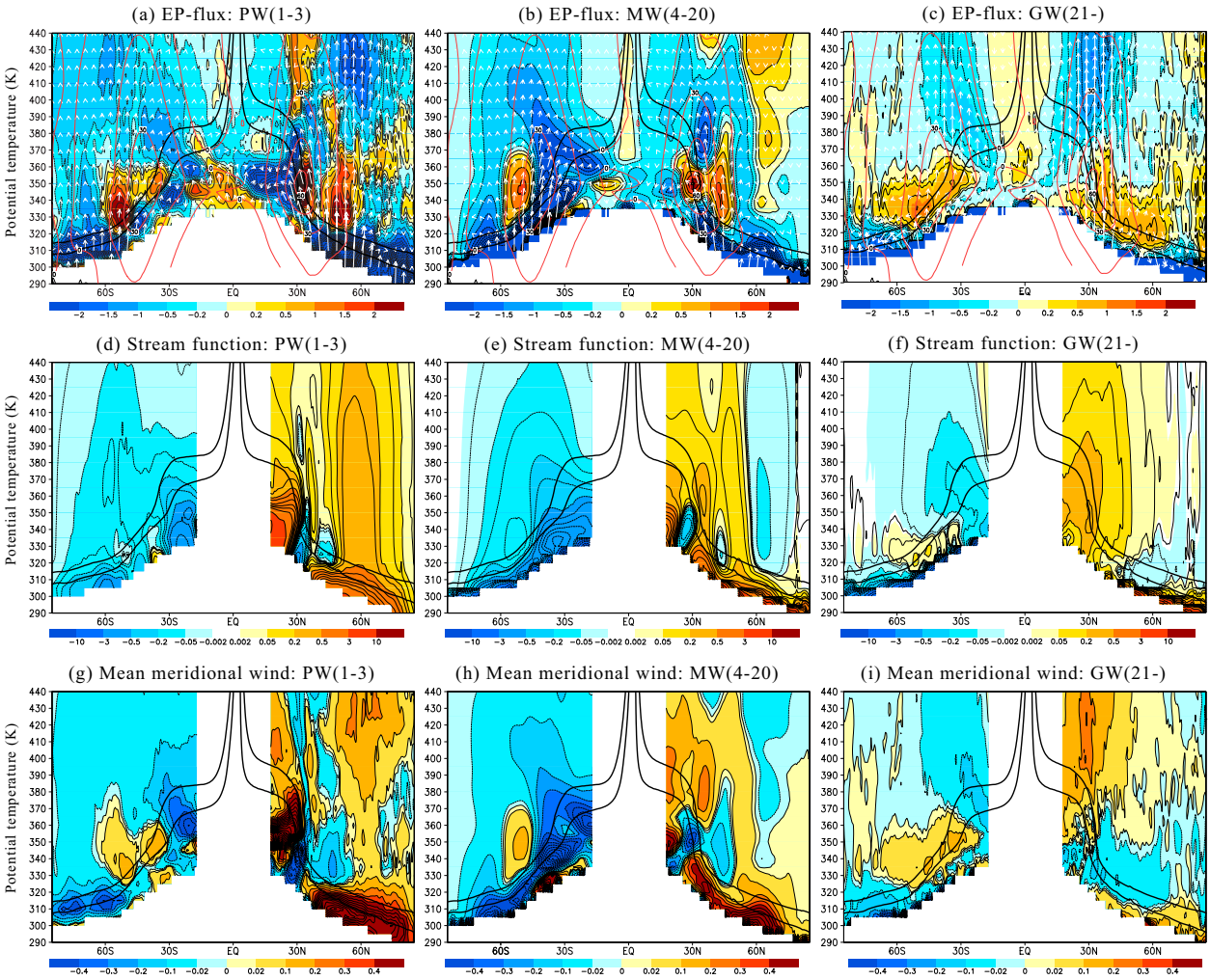

FIG. 1. Latitude-potential temperature cross section of monthly mean (top) E-P flux vectors (arrows) and E-P flux divergence (in $ms^{-1}day^{-1}$, shaded color with thin black contour lines) together with zonal mean zonal wind (red contour lines, with intervals of 15 ms^{-1}), (middle) mass streamfunction (in $10 \times 10^{10} kgs^{-1}$, shaded colors with thin black contour lines), and (lower) mean meridional wind velocity (in ms^{-1}) for January. The mass streamfunction and mean meridional wind velocity were estimated from the downward control calculation using the E-P flux divergence. These are associated with (left) the zonal wavenumbers 1-3, (middle) the total horizontal wavenumbers 1-20 except for the zonal wavenumbers 1-3, and (right) the total horizontal wavenumbers 21-213. The bold black contour lines represent the absolute values of PVU at 2 and 4 PVU.

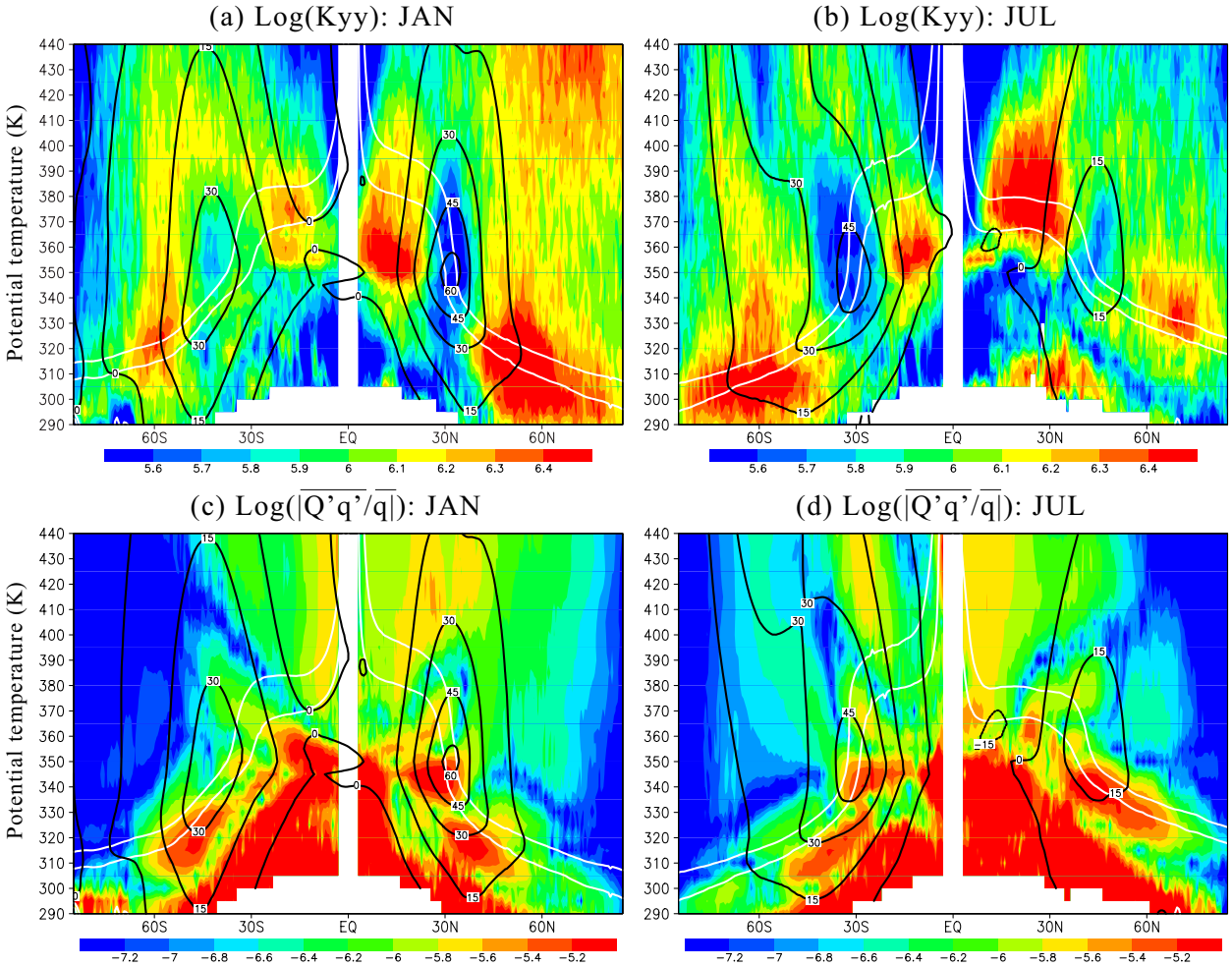

FIG. 2. Latitude-potential temperature cross section of the logarithms of the isentropic diffusion coefficient (K_{yy}, in $m^2 s^{-1}$, upper panels) and the vertical diffusion coefficient ($\frac{\overline{Q'q'}}{\overline{q}}$, in Ks^{-1}, lower panels) for January (left panels) and July (right panels). The black contour lines represent the zonal mean zonal wind with intervals of 15 ms^{-1}. The white contour lines represent the absolute values of PVU at 2 and 4 PVU.

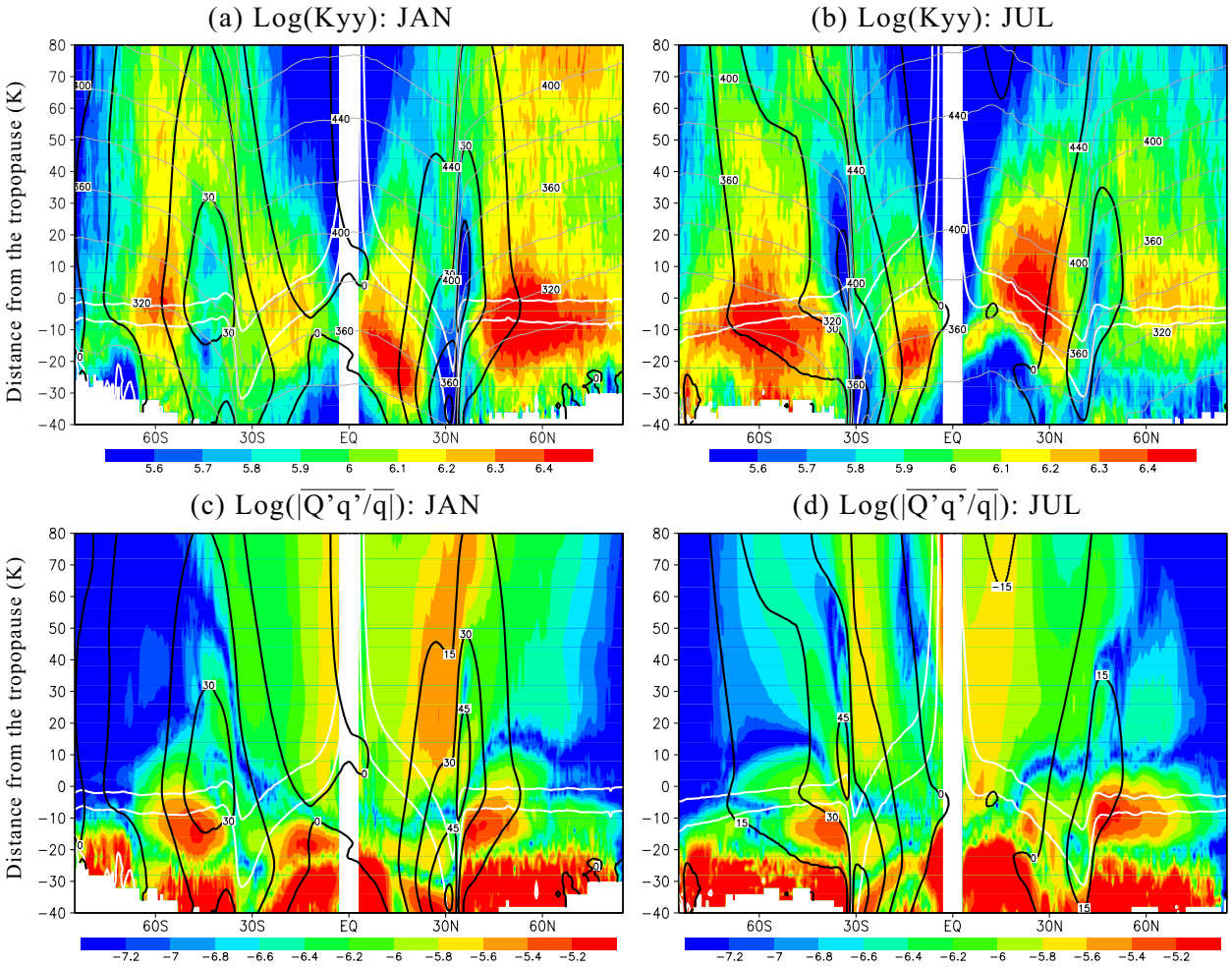

FIG. 3. The same as Fig. 2, but as a function of latitude and distance from the thermal tropopause ($\Delta\theta_{TP}$). The gray contour lines represent the potential temperature with intervals of 20 K.

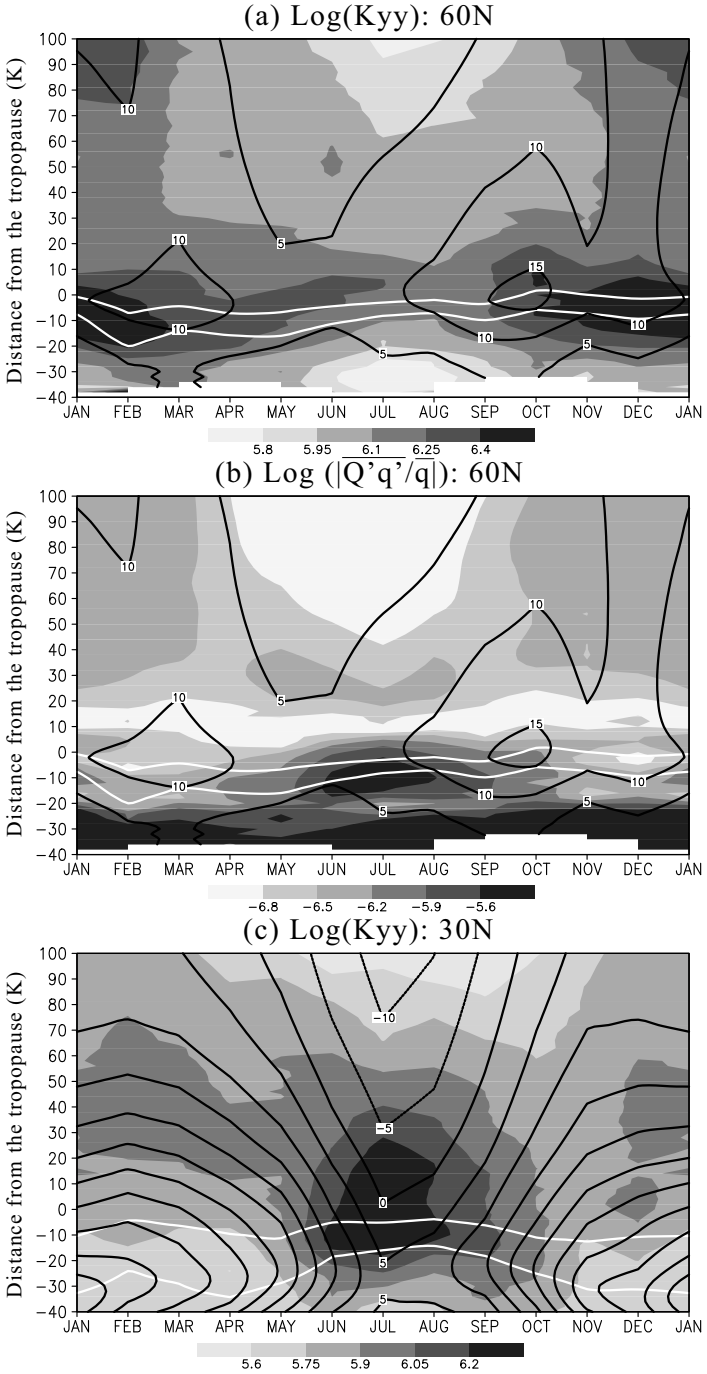

FIG. 4. Seasonal variation of (a, c) the logarithms of the isentropic diffusion coefficient (K_{yy}, in $m^2 s^{-1}$) and (b) the vertical diffusion coefficient ($\frac{\overline{Q'q'}}{\overline{q}}$, in Ks^{-1}) at (a, b) 60 N and (c) 30 N, as a function of the distance from the thermal tropopause ($\Delta\theta_{TP}$). The black contour lines represent the zonal mean zonal wind with intervals of 5 ms^{-1}. The white contour lines represent the absolute values of PVU at 2 and 4 PVU.

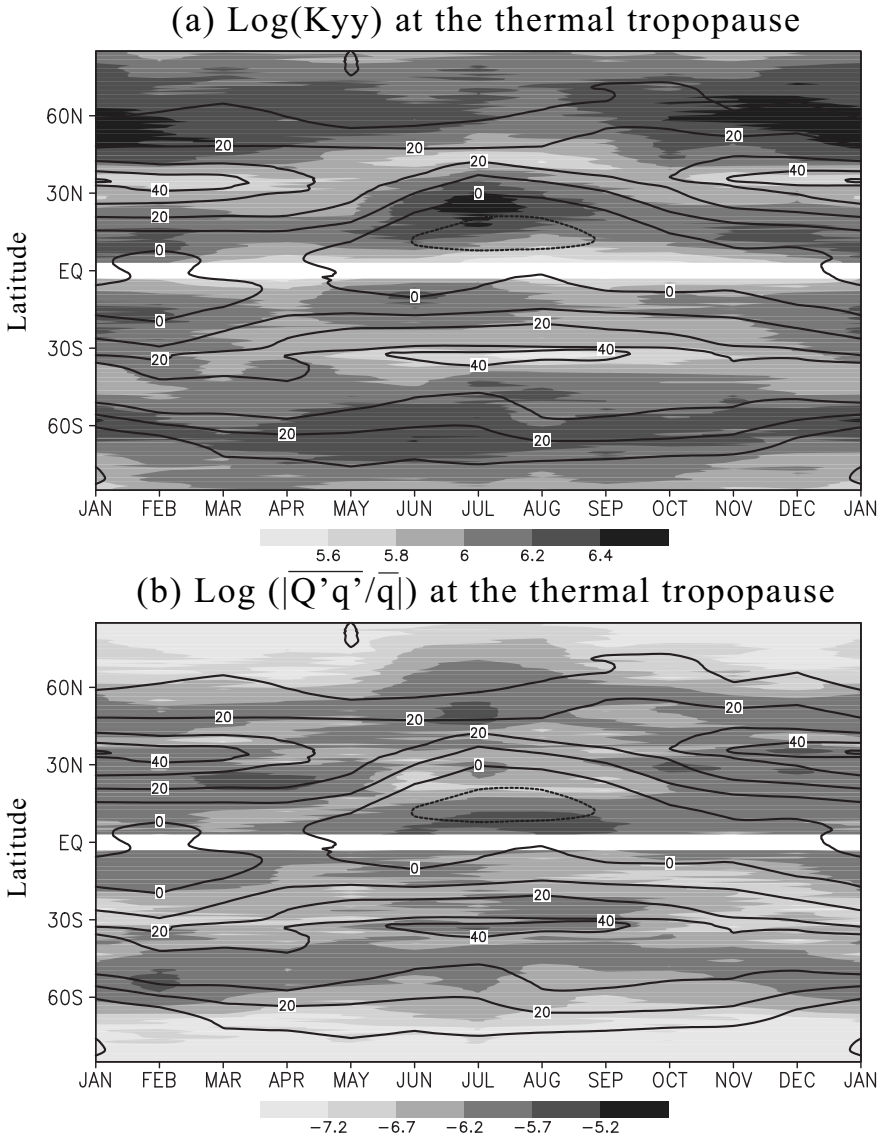

FIG. 5. Seasonal variation of (a) the logarithms of the isentropic diffusion coefficient (K_{yy}, in $m^2 s^{-1}$) and (b) the vertical diffusion coefficient ($\frac{\overline{Q'q'}}{\overline{q}}$, in Ks^{-1}) at the thermal tropopause height ($\Delta\theta_{TP}$=0). The black contour lines represent zonal mean zonal wind with intervals of 10 ms^{-1}.

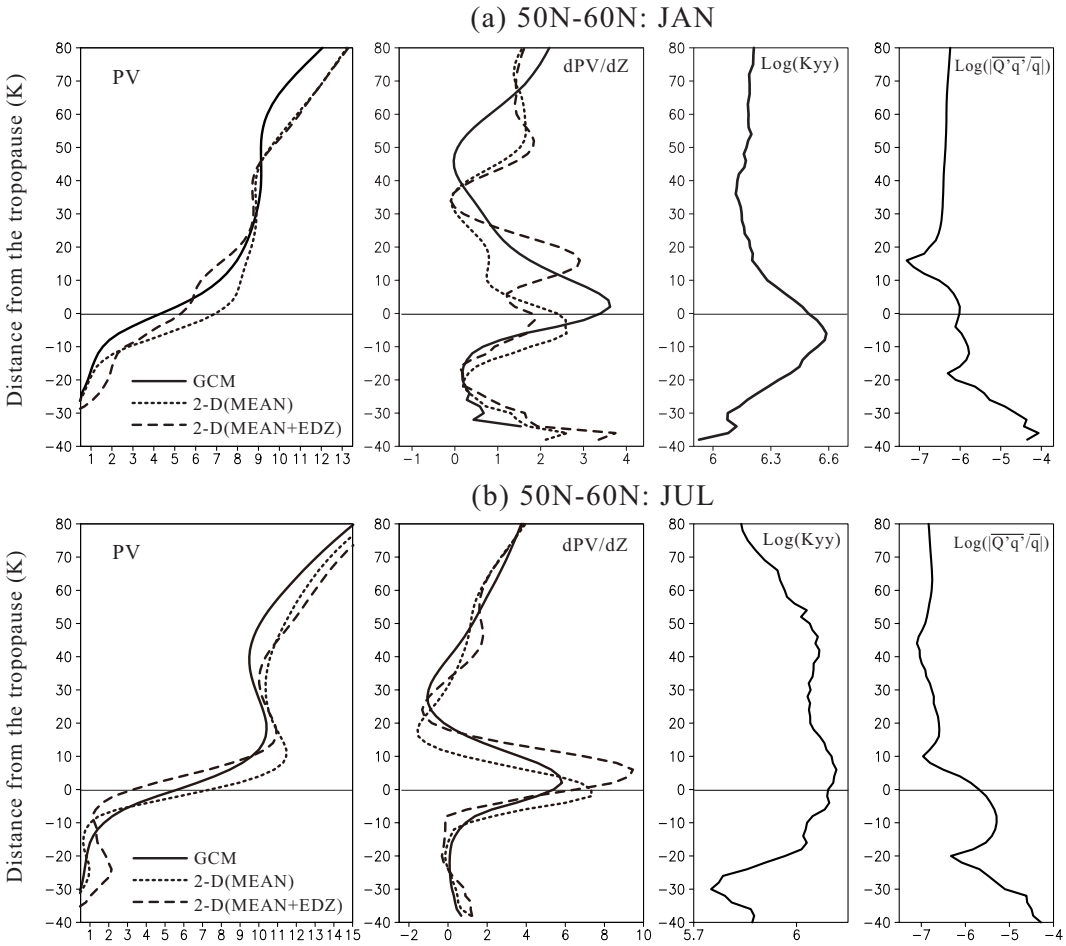

FIG. 6. Vertical profiles of PV value (first column), vertical PV gradient (in $PVUkm^{-1}$, second column), and the logarithm of Kyy (in m^2s^{-1}, third column) and the vertical diffusion coefficient ($\frac{\overline{Q'q'}}{\bar{q}}$, in Ks^{-1}, forth column), as functions of the distance from the thermal tropopause ($\Delta\theta_{TP}$) average between 50 N and 60 N, during (a) January 14th-20th and (b) July 14th-20th, obtained from the GCM simulation (solid line), the 2-D model calculation that neglected both the eddy meridional and vertical transport terms (dotted line), and the 2-D model calculation that only neglected the eddy meridional transport term (dashed line).

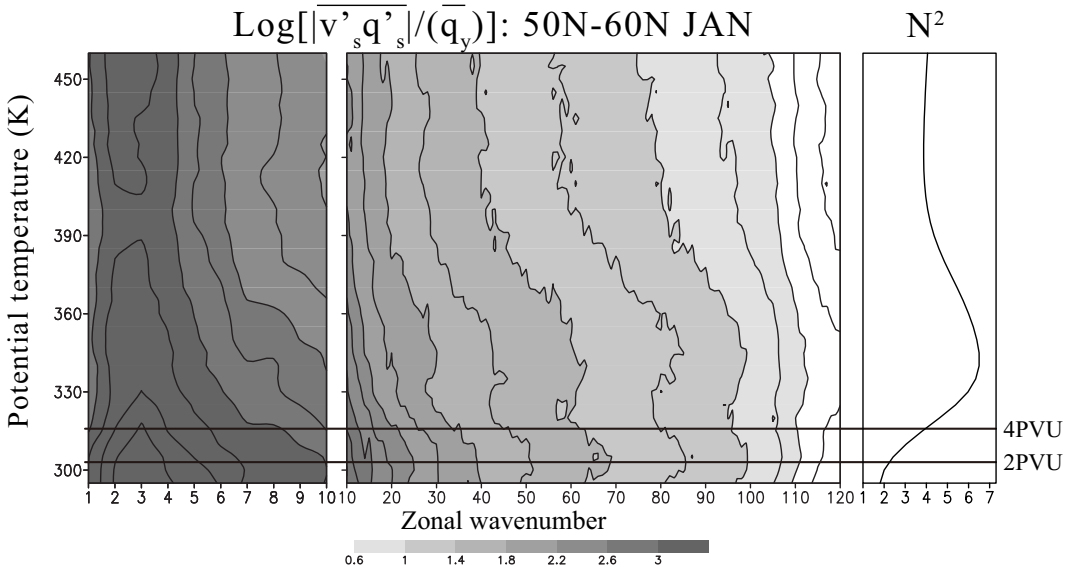

FIG. 7. Zonal wavenumber-potential temperature cross section of isentropic eddy PV flux normalized by background PV gradient (in $m^2 s^{-1}$) averaged between 50 N and 60 N in January. The straight lines represent the absolute values of PVU at 2 and 4 PVU. Note the different scaling used in the different panels of the figure. The right panels show the monthly mean N^2 profiles (in $10^{-4} s^{-2}$).

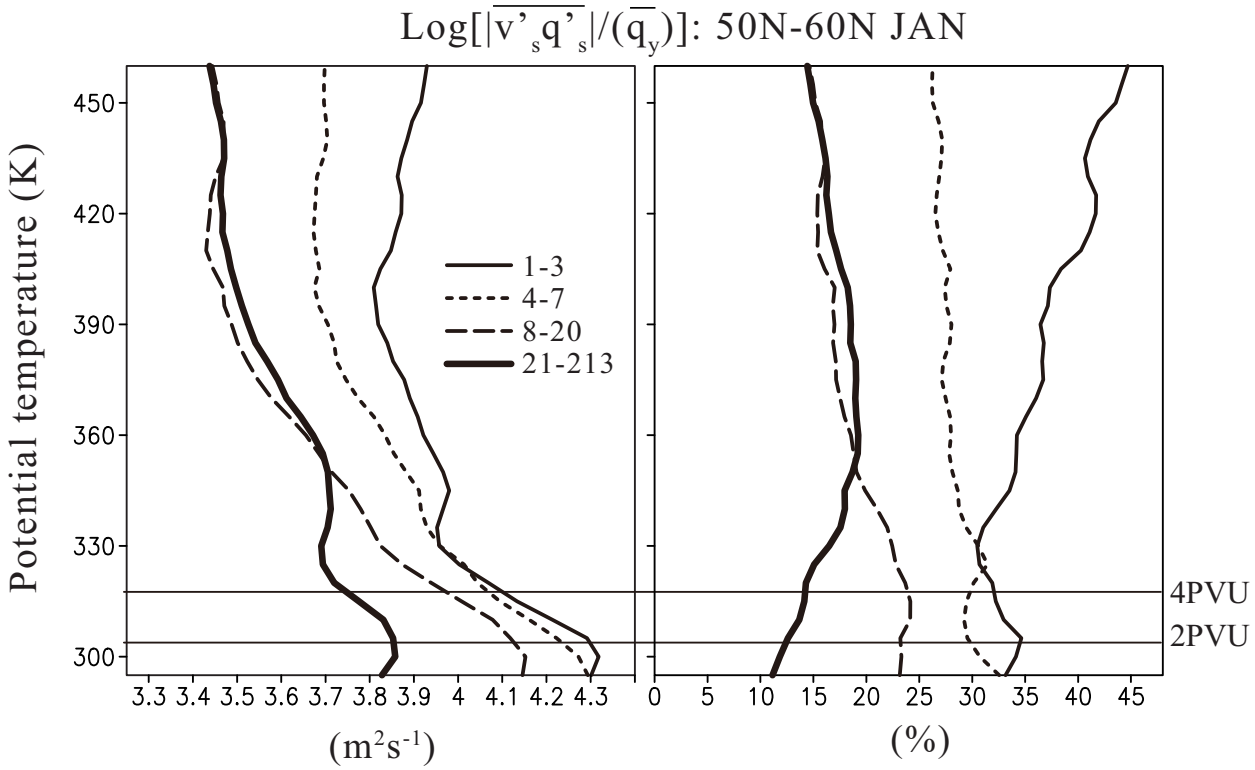

FIG. 8. Relative contributions of different wave components to isentropic eddy PV flux normalized by background PV gradient in $m^2 s^{-1}$ (left) and in % (right) averaged between 50 N and 60 N in January. These are associated with the zonal wavenumbers 1-3 (thin solid line), 4-7 (dotted line), 8-20 (broken line), and 21-213 (bold solid line). The straight lines represent the PVU values at 2 and 4 PVU.

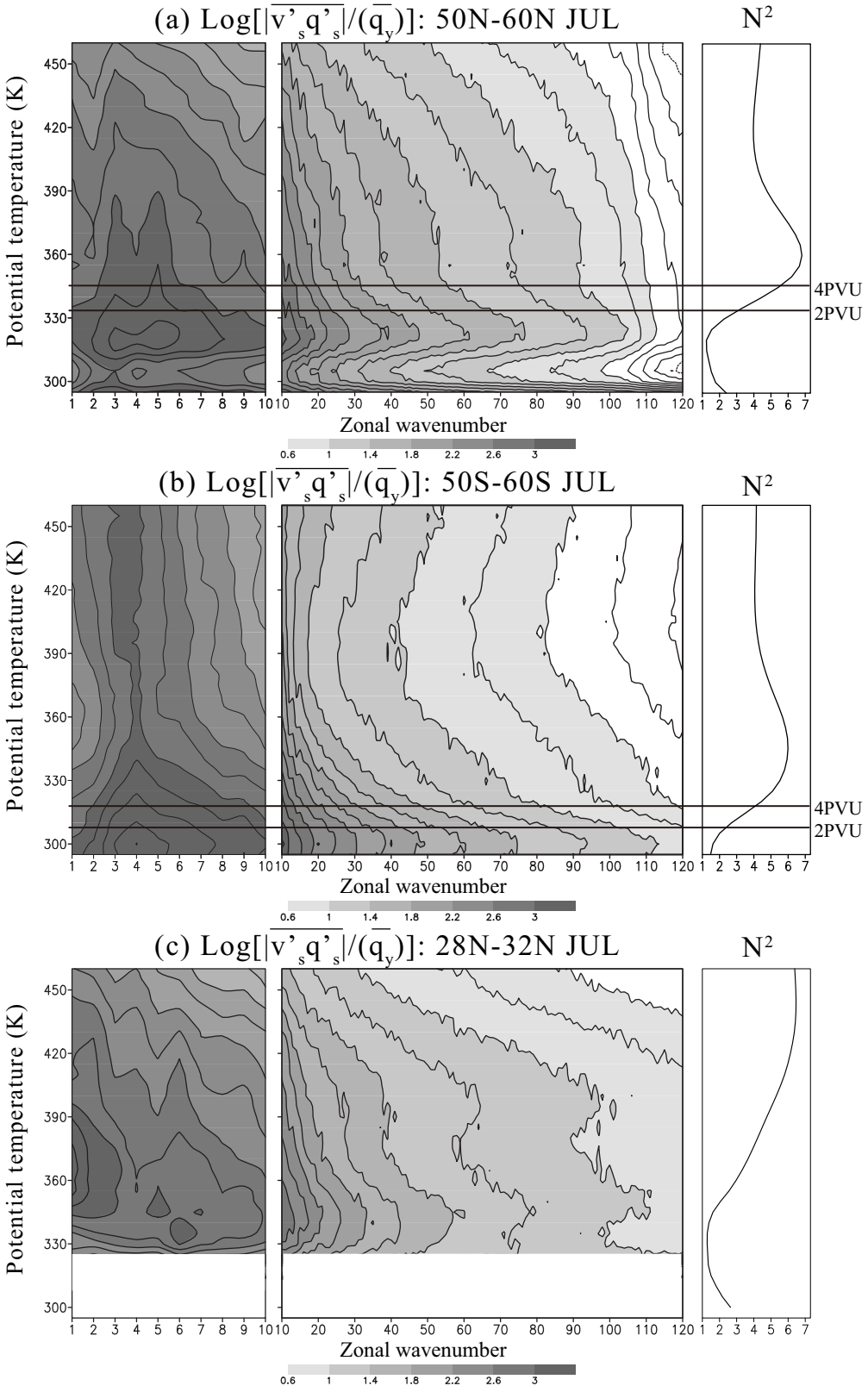

FIG. 9. The same as Fig. 7, but averaged between (a) 50 N and 60 N in July, (b) 50 S and 60 S in July, and (c) 28 N and 32 N in July. Note the different scaling used in the different panels of the figure.

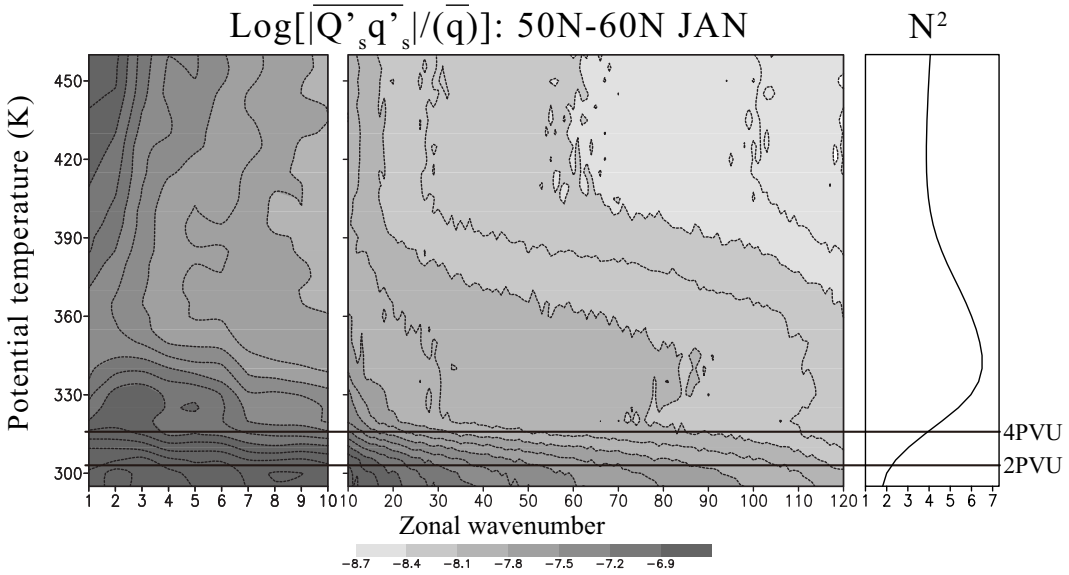

FIG. 10. The same as Fig. 7, but for the eddy vertical PV flux normalized by the background PV value (in Ks^{-1}) averaged between 50 N and 60 N in January. Note the different scaling used in the different panels of the figure.

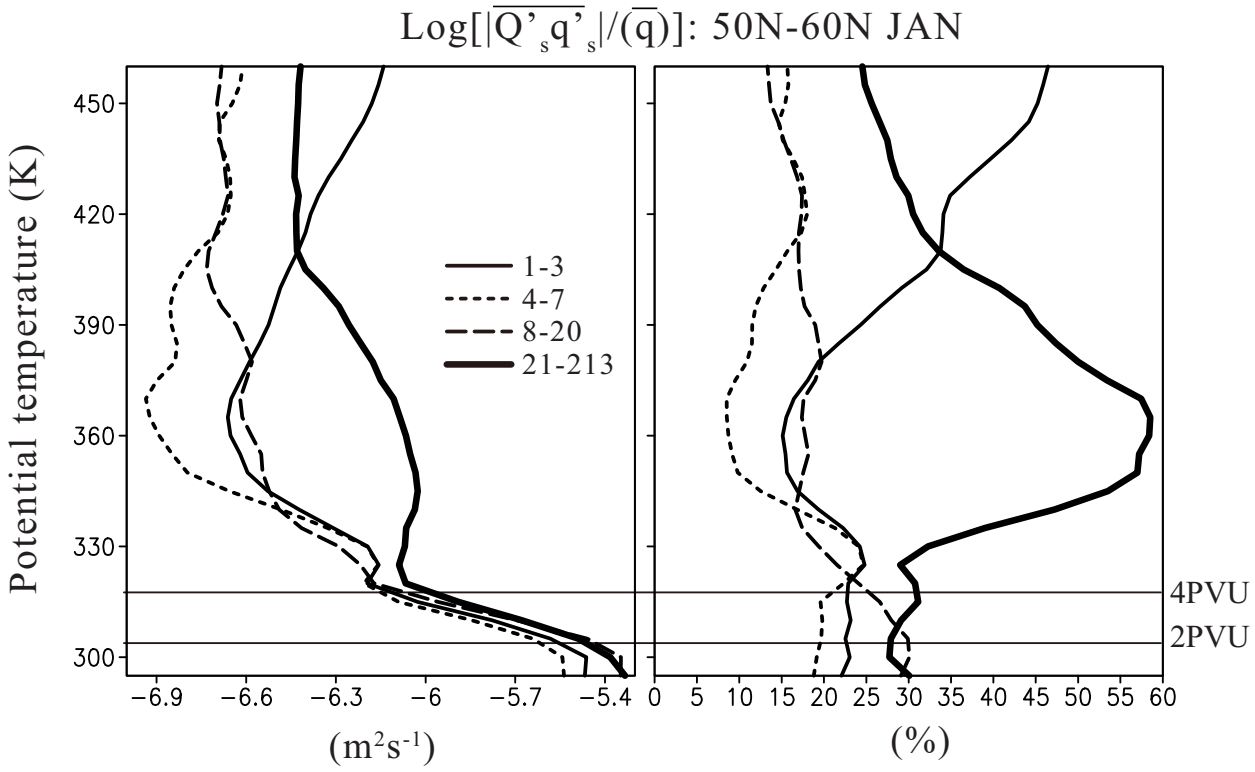

FIG. 11. The same as Fig. 8, but for the relative contributions of the different wave components to the vertical eddy PV flux normalized by the background PV value averaged between 50 N and 60 N in January.

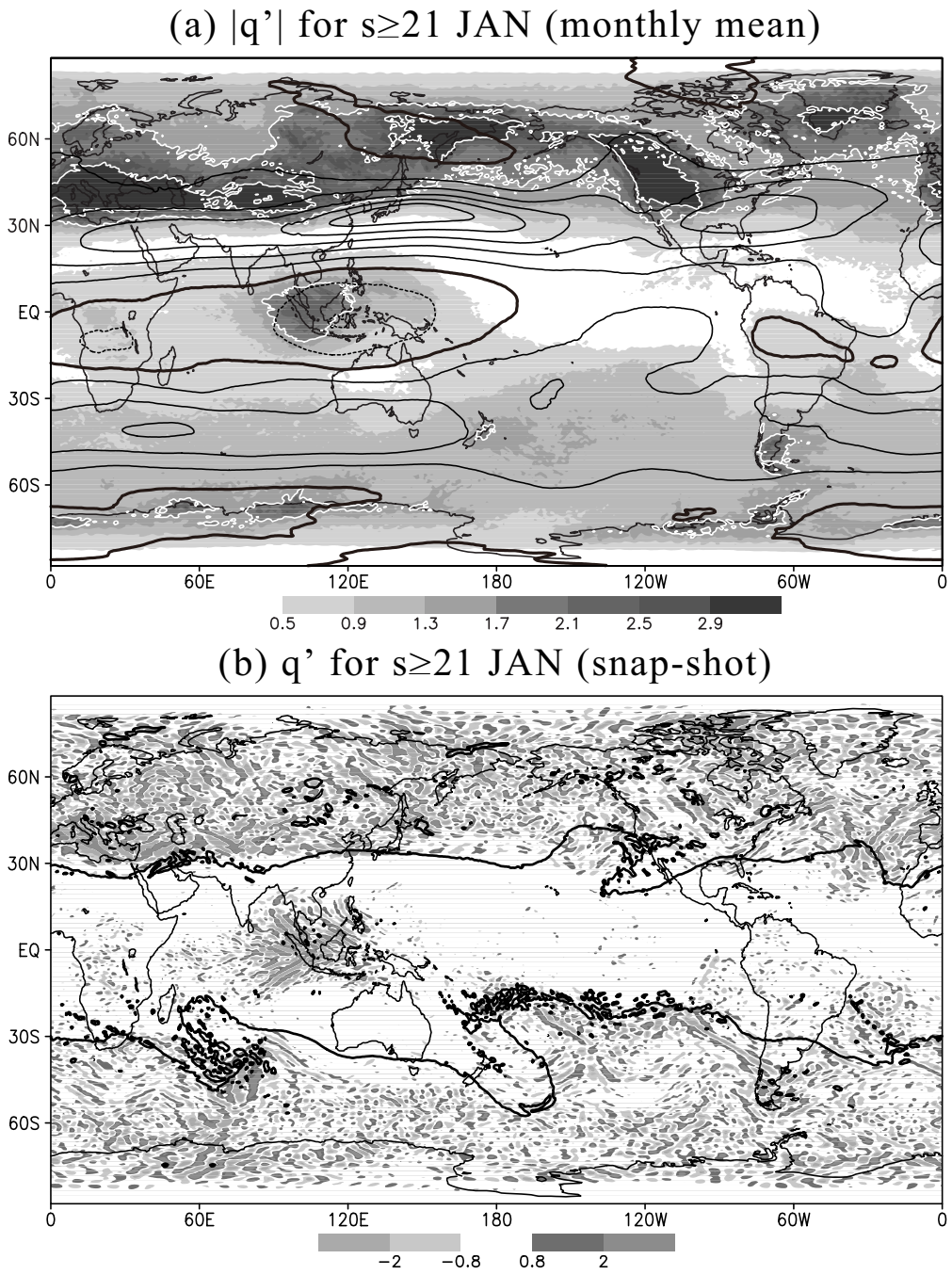

FIG. 12. Spatial distributions of small horizontal-scale PV disturbances (in PVU) with zonal wavenumbers ≥ 21 on 360 K surface, (a) monthly mean amplitude and (b) snapshot distribution. The black contour lines in (a) represent the zonal mean zonal wind with intervals of 15 ms^{-1}; the bold lines represent zero zonal wind; the dotted lines represent easterly wind. The white contour lines in (a) represent the monthly mean amplitudes of the PV disturbances at 1.7 and 2.9 PVU. The black contour lines in (b) represent the dynamical tropopause (i.e., -4 or 4 PVU).

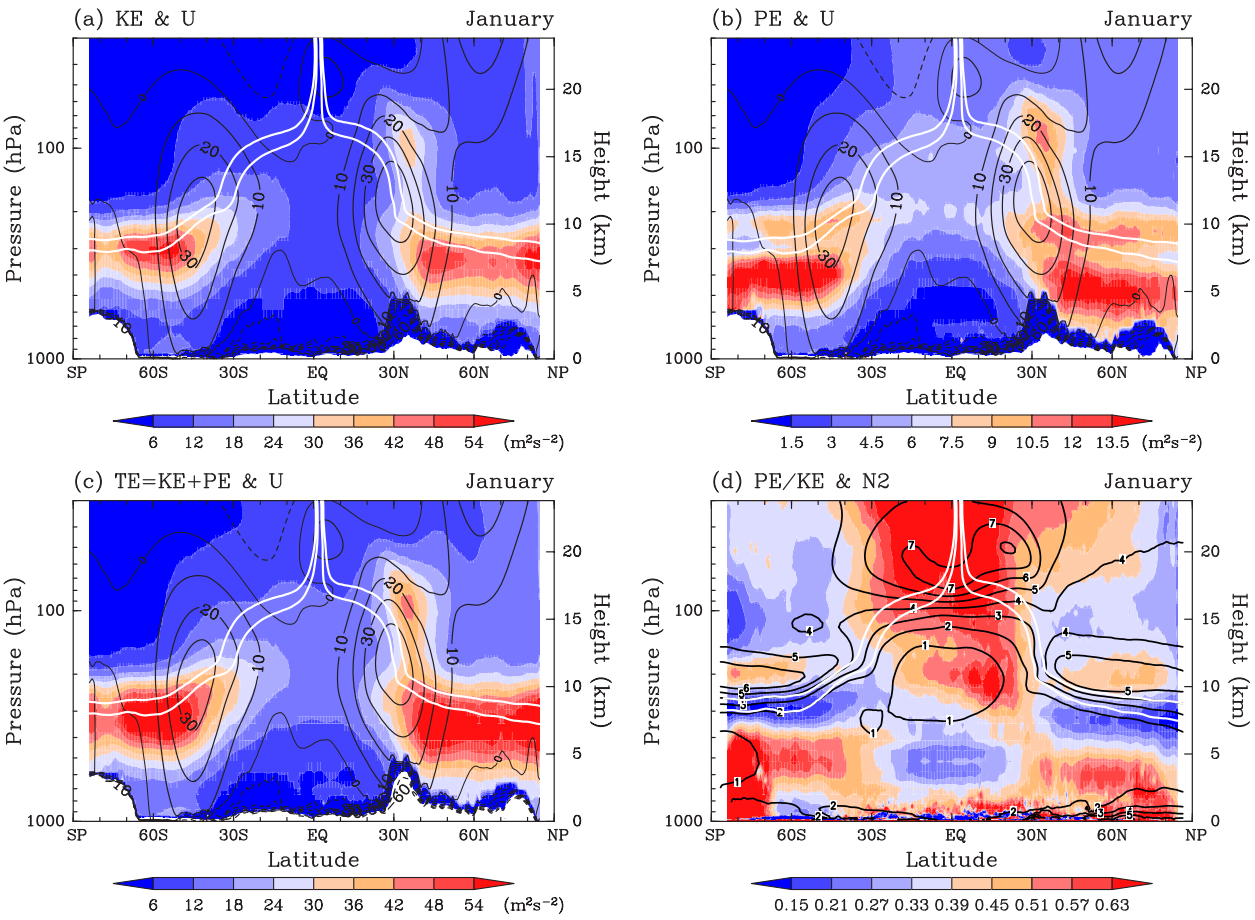

FIG. 13. Latitude-pressure cross section of (a) kinetic energy (KE), (b) potential energy (PE), and (c) total energy (TE = PE + KE) of gravity waves for January. The relative ratio of PE to KE (PE/KE) is shown in (d). The black contour lines show the zonal mean zonal wind with intervals of 10 ms^{-1} in (a-c) and N^2 with intervals of $10^{-4}s^{-2}$ in (d). The white contour lines represent the absolute values of PVU at 2 and 4 PVU.

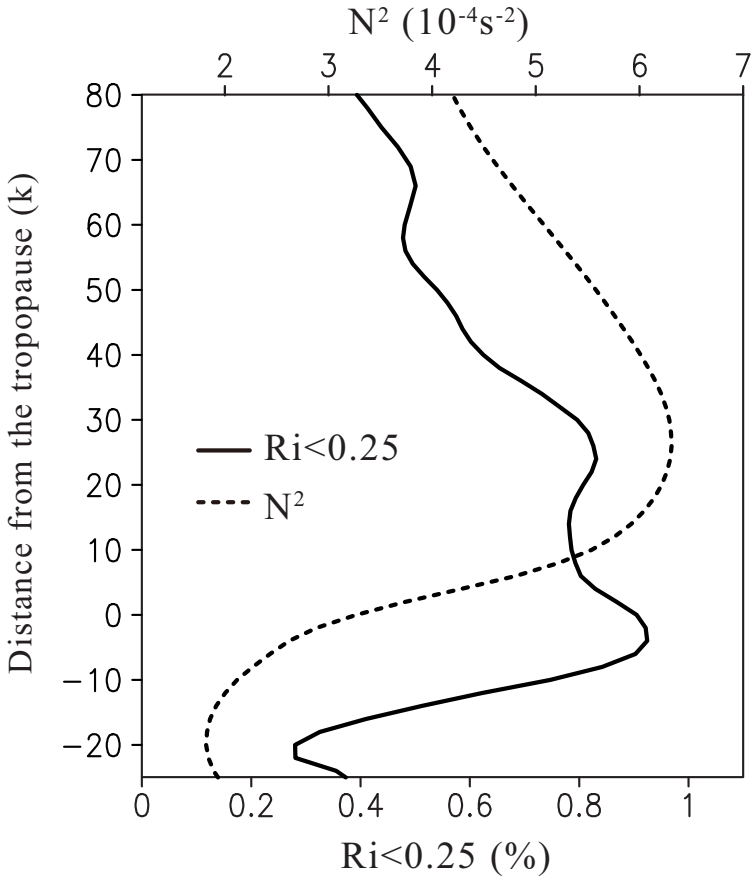

FIG. 14. Vertical profile of probability of the occurrence of Ri < 0.25 (solid line) and Buoyancy frequency squared, N^2 (broken line), at 60 N for January, obtained from the T213L256 GCM output, as a function of the distance from the thermal tropopause (in potential temperature).

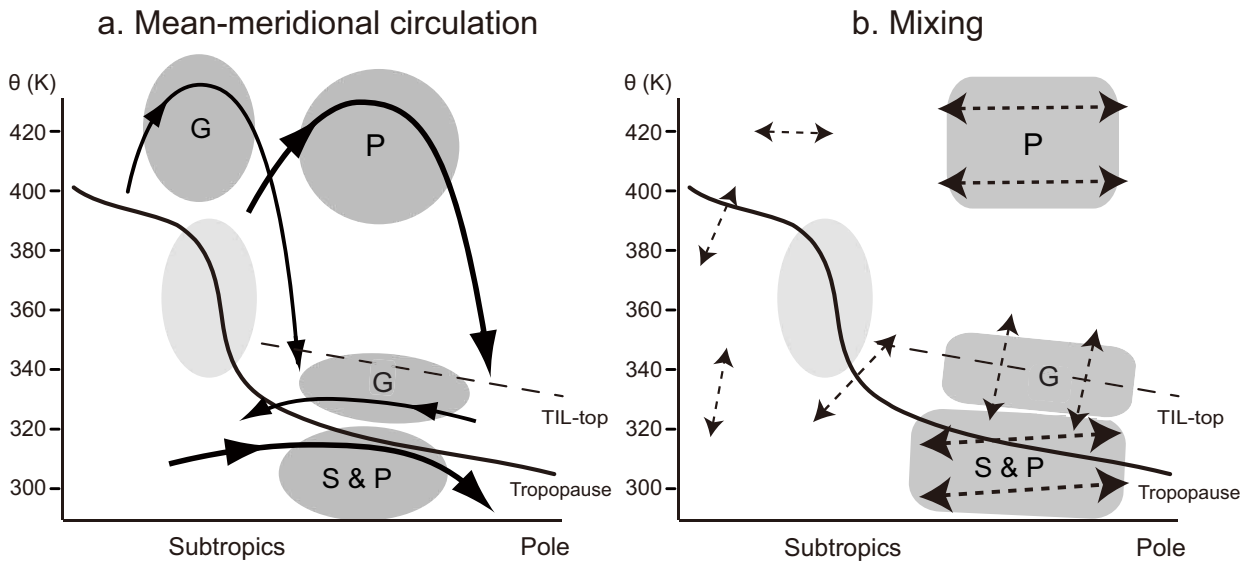

FIG. 15. Schematic diagram of (a) transport and (b) mixing in the extratropical UTLS for the winter hemisphere. Straight arrows indicate transport due to the mean-meridional circulation in (a); double-headed arrows with broken lines indicate transport by eddies (mixing) in (b). The labels "P," "S," and "G" denote dominant scales for transport and mixing for planetary-, synoptic-, and gravity-wave-scale, respectively. The shaded circles and squares represent regions of large E-P flux convergence (or divergence) in (a) and strong mixing in (b), respectively. The solid line represents the dynamical tropopause; the broken line represents the upper boundary height of the TIL; the light shaded area represents the subtropical westerly jet.